Cryogenic payloads for the Einstein Telescope: Baseline design with heat extraction, suspension thermal noise modeling, and sensitivity analyses

Xhesika Koroveshi,[1,2,*] Lennard Busch,[1] Ettore Majorana,[3,4] Paola Puppo,[3] Piero Rapagnani,[3,4] Fulvio Ricci,[3,4] Paolo Ruggi,[5] and Steffen Grohmann[1,2]

[1]*Institute of Technical Thermodynamics and Refrigeration, Organizational Unit: Refrigeration and Cryogenics, Karlsruhe Institute of Technology, 76131 Karlsruhe, Germany*
[2]*Institute of Beam Physics and Technology, Karlsruhe Institute of Technology, 76344 Eggenstein-Leopoldshafen, Germany*
[3]*INFN, Sezione di Roma, I-00185 Roma, Italy*
[4]*Dipartimento di Fisica, Università degli studi di Roma "La Sapienza", I-00185 Roma, Italy*
[5]*European Gravitational Observatory, I-56021 Cascina, Italy*

(Received 23 May 2023; accepted 11 August 2023; published 7 December 2023)

The Einstein Telescope (ET) is a third-generation gravitational wave detector that includes a room-temperature high-frequency (ET-HF) and a cryogenic low-frequency laser interferometer (ET-LF). The cryogenic ET-LF is crucial for exploiting the full scientific potential of the ET. We present a new baseline design for the cryogenic payload that is thermally and mechanically consistent and compatible with the design sensitivity curve of the ET. The design includes two options for the heat extraction from the marionette, based on a monocrystalline high-conductivity marionette suspension fiber and a thin-wall titanium tube filled with static He-II. Following a detailed description of the design options and the suspension thermal noise (STN) modeling, we present the sensitivity curves of the two baseline designs, discuss the influence of various design parameters on the sensitivity of ET-LF, and conclude with an outlook to future R&D activities.

DOI: 10.1103/PhysRevD.108.123009

I. INTRODUCTION

The Einstein Telescope (ET) is a third-generation gravitational wave (GW) detector with a xylophone design, combining a low-frequency (LF) and a high-frequency (HF) laser interferometer. Sensitivities lie in the ranges of 3 Hz to 30 Hz (ET-LF) and 30 Hz to 10 kHz (ET-HF), respectively. The low-frequency sensitivity is crucial for exploiting the full scientific potential of ET, in particular with regard to:

(1) the observation of binary neutron stars (BNSs), staying a long time in the bandwidth,
(2) premerger detection to probe the central engine of gamma-ray bursts (GRBs), particularly to understand the jet composition, the particle acceleration mechanism, and the radiation and energy dissipation mechanisms,
(3) detecting a large number of kilonova counterparts,
(4) detecting primordial black holes (PBHs) at redshifts $z > 30$,
(5) detecting intermediate massive back holes (IMBHs) in the range of 10^2–$10^4 M_\odot$ [1].

Figure 1 shows the noise contributions to the sensitivity curve ET-D [2], based on payload design parameters listed in Table I. Cryogenic operation of the payload is indispensable to suppress the suspension thermal noise (STN) to the level of gravity gradients—i.e., Newtonian noise (NN). Both STN and NN are the fundamental noises that dominate the ET-LF noise budget at frequencies below 10 Hz.

The technical implementation of the parameters in Table I is not straightforward [3,4]. Therefore, in this paper we develop a baseline design of a cryogenic payload for ET-LF, which is consistent in terms of mechanical and thermal design, as well as STN modeling. It shall serve as a stepping stone for the cryostat design and for future payload design optimization, rather than assuming it to be "final." The focus of this paper is purely on the payload, not yet including the impact of cooling interfaces, which is a subject of future R&D.

Section II introduces the baseline cryogenic payload design for ET-LF with two heat extraction concepts, which are further explained in Secs. III and IV. This is followed in Sec. V by a detailed description of the STN modeling. Section VI then presents the sensitivity curves of the

*xhesika.koroveshi@kit.edu

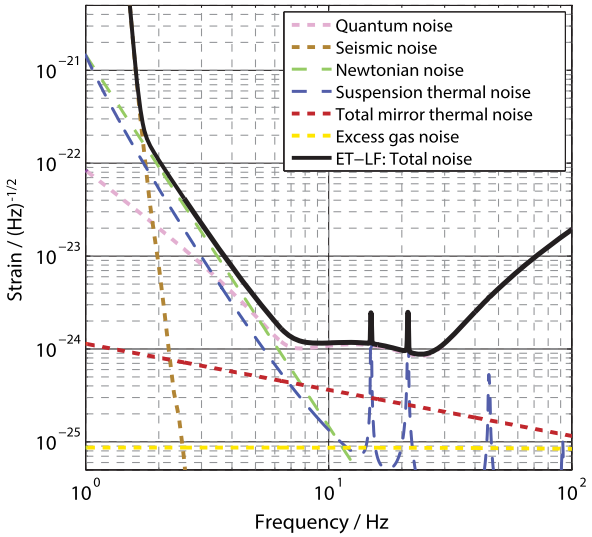

FIG. 1. ET-LF noise contributions in the ET-D sensitivity curve [2].

baseline designs. The influence of various design parameters on the sensitivity of ET-LF is analyzed in Sec. VII, before main conclusions and an outlook to future R&D activities are presented in Sec. VIII.

II. BASELINE DESIGN OF A CRYOGENIC PAYLOAD FOR ET-LF

A. Overall operating conditions

ET-LF shall be operated with a 1550 nm wavelength laser at an arm power of 18 kW. The baseline material for the mirror and its suspension fibers is monocrystalline silicon. An alternative material for the mirror and its suspensions is sapphire. The operating temperature of the mirror is between 10 K and 20 K. While a 0.1 W heat load has been estimated in [2,5], we redefine an engineering design target of

$$\dot{Q} = 0.5 \text{ W} \tag{1}$$

total heat load on the ET-LF payload, considering the size and complexity of the cryostat and including the need for optical access. This value entails a thermal safety margin and compares to a range of 0.5–1.0 W that KAGRA, the first cryogenic gravitational wave detector, assumes on its cryogenic test masses of 23 kg, partially caused by a higher absorption in its sapphire mirrors [6].

TABLE I. ET-LF payload design parameters from [2], using a branched pendulum model as in Virgo.

	Marionette	Recoil mass	Mirror
Mass (kg)	422	211	211
Suspension length (m)	2	2	2
Suspension diameter (mm)	3	3	3
Suspension material (-)	Ti6Al4V	Silicon	Silicon
Loss angle (-)	1×10^{-5}	1×10^{-8}	1×10^{-8}
Temperature (K)	2	10	10

B. Conceptual design of the payload

The baseline design of the ET-LF cryogenic payload is derived from the double pendulum layout of the Advanced Virgo (AdVirgo) payload [7]. It is depicted in Fig. 2 and includes the following main components:

(1) *Platform* (PF), from which the marionette and the cage are suspended separately, using a single suspension for the marionette and three suspensions for the cage. The platform is the first stage inside the ET-LF cryostat volume, being suspended from a warm superattenuator system.
(2) *Marionette* (MA), which coordinates the position of the mirror via four monocrystalline silicon suspension fibers. These suspensions are connected to so-called mirror ears that are attached via hydroxide catalysis bonding (HCB) onto the sides of the mirror.
(3) *Actuation cage* (CA), which serves as a reaction mass for both the mirror and the marionette. In addition, various sensory devices are installed on this robust structure to avoid a direct contact with the sensitive optics. In AdVirgo, the cage is rigidly attached to the PF, whereas a suspended cage is proposed here.
(4) *Mirror / Test mass* (MI), which constitutes the core optical element of the interferometer.

The design of the cryogenic payload must consider thermal and mechanical feasibility, while fulfilling a low STN contribution compatible with the ET-D sensitivity

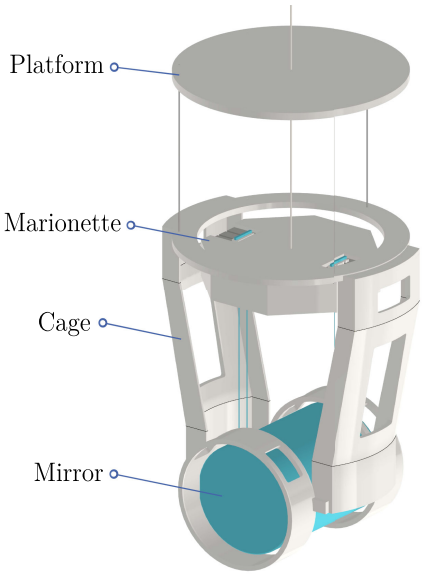

FIG. 2. Baseline design of the ET-LF cryogenic payload based on the AdVirgo double pendulum design.

TABLE II. Baseline design parameters of the ET-LF payload, including two marionette cooling concepts.

	Marionette			Mirror	
Cooling concept	Monolithic	Monolithic	He-II filled	Silicon	Sapphire
Mass (kg)	200	220	200	200	220
Suspension length (m)	1.0	1.0	1.0	1.2	1.2
Suspension diameter (mm)	8.1	6.5	8.3	3.0	2.3
Suspension material (-)	Silicon	Sapphire	Ti, He-II	Silicon	Sapphire
Bulk loss angle (-)	1×10^{-9}	3×10^{-9}	1×10^{-6}	1×10^{-9}	3×10^{-9}
Temperature (K)	15	17	2	15…20	20…23

curve [2]. The correct implementation of interfaces, temperature gradients, and mechanical safety factors is essential. Further design aspects include the cryostat dimensions and space requirements for installation and auxiliary systems, the fabrication of long and high-quality monocrystalline suspension fibers, and the achievable marionette temperature based on the cooling concept.

The AdVirgo payload operating at room temperature has a MA made of 316L stainless steel [7]. In the ET-LF cryogenic payload, the material for the MA remains to be decided. In addition to mechanical functionality, the choice is influenced by thermal aspects—i.e., the transient cool-down behavior and the achievable temperatures in steady-state operation. Therefore, aluminum alloys offer an alternative material choice for the MA.

The combination of various constraints yields the baseline design parameters listed in Table II. While the mirror suspensions are generally made of monocrystalline silicon or sapphire fibers, we propose two alternative concepts for the heat extraction and the marionette suspension. The first concept presented in Sec. III relies on a cooling interface on the CA and the PF, requiring a monocrystalline high-conductivity marionette suspension made of silicon or sapphire. The second concept uses a thin-wall titanium tube as a marionette suspension that is filled with superfluid He-II. This concept provides cooling at 2 K down to the marionette and is explained in Sec. IV. In both heat extraction concepts, the cooling interface design will affect the sensitivity. Defining the interface deteriorative impact on sensitivity and thermal resistivity requires a refined and experimental-based analysis. The designs will result from experimental investigation and optimization, which are not yet advanced enough to be included in the scope of this paper.

III. CONCEPT WITH MONOCRYSTALLINE MARIONETTE SUSPENSION

A. Motivation

The initial conceptual payload design with the parameters in Table I is based on a heat extraction interface on the marionette, which is thermally insulated from the platform via a low-conductivity Ti6Al4V suspension [2]. STN computations [8,9] reveal that the cooling interface must be implemented on the CA and passed to the PF, as the direct connection of any high-dissipation cooling path on the marionette would critically affect the thermal noise. Hence, the suspension material must induce low STN and provide high thermal conductivity and mechanical strength. Al6N can be used to connect the payload to the cryogenic system, but is not an option to suspend the marionette due to a very low yield strength [10], which is more than 1 order of magnitude smaller compared to crystalline silicon or sapphire. The low STN requirement is achieved for crystalline sapphire and silicon at low temperatures thanks to their high quality factor Q [11], where Q is the inverse of the loss angle ϕ at resonance [12,13], cf. Sec. V.

The overall results from the computations converge in the assessment that the marionette suspension mechanics must assure low thermal noise—i.e., mechanical dissipation—in order to preserve ET-LF sensitivity goals. The most advanced toy model takes into account the presence of soft Al6N thermal links, similar to those implemented in KAGRA [14–16], connecting the CA to the thermal shield, combined with a heat extraction through the PF via a crystalline marionette suspension fiber with high Q and high thermal conductivity. The payload and cryostat dimensions, as well as the sensitivity goal in ET-LF, differ from KAGRA, implying differences in the thermal and mechanical design requirements [5,6], which are not straightforward to define.

Figure 3 depicts the examined thermal link interface possibilities on the cryogenic payload. A simple double-stage payload with sapphire marionette and mirror suspensions is used as a reference. In the simplest case (left), the thermal link (TL) to the cryogenic system is modeled by a connection to the MA, showing up critical impact on the predicted sensitivity. A more realistic case (right) adopts a connection onto the CA and PF, ensuring sustainable mechanics of the TL connection. Figure 4 shows the effect of the soft thermal link on the STN for the cases depicted in Fig. 3. Imposing a nominal assumption for the STN roughly comparable with that of ET-LF, it can be realized that the TL should be connected far from the MI. Figure 4 demonstrates that the thermal links must be connected to the CA, being the minimum distance from the MI in order

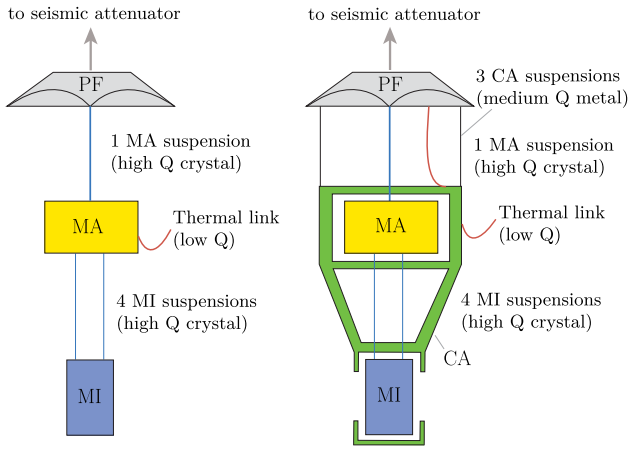

FIG. 3. Schemes of thermal link connection possibilities onto the cryogenic payload.

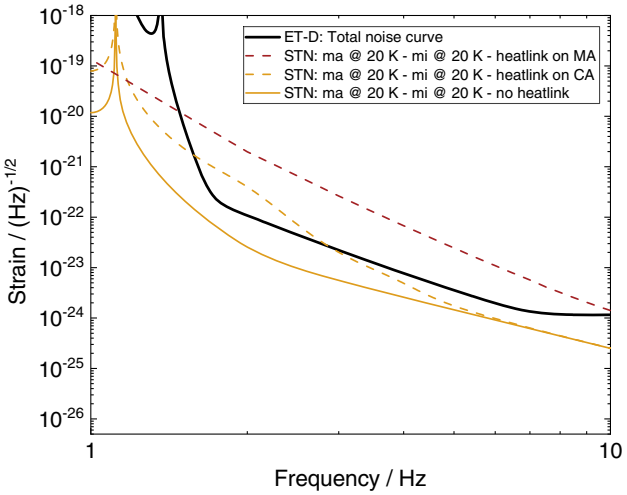

FIG. 4. Impact on the STN due to a direct connection of a 1 m thermal link (made of 28 braids, each composed by 49 Al6N wires with $d = 150$ μm [14] and assuming $\phi_{TL} = 0.5$) on the MA and CA.

not to compromise the STN. The criticality is reached with the parameters mentioned in the caption of Fig. 4. The computation is analytic, but FEA modeling provides similar results [4,17]. A secondary but yet significant issue is the noise injection and the drag through the thermal link, which has been estimated with a similar method as in Fig. 4 [8].

The outline of the solid conduction cooling through thermal links is that in order to reduce the thermal noise (cf. Sec. V) induced from the link, it must be connected to the CA and cannot reach the MA. The implementation is feasible through a careful mechanical and thermal design of the payload in order to operate at $T_{MI} \approx 20$ K. The monocrystalline-based concept in this paper assumes using the same material (silicon or sapphire) for the mirror, the mirror suspensions, and the marionette suspension. Nonetheless, also a hybrid monocrystalline suspension application is being analyzed [18,19].

B. Mechanical dimensioning

The marionette suspension is dimensioned for the total mechanical load of the MA and the MI, considering a safety factor SF = 3 with regard to the ultimate strength σ_{max}. The material properties listed in Table III for sapphire and silicon yield the dimensions in Table II, which are used in the STN modeling in this paper. For sapphire, a very conservative value of 400 MPa is assumed, based upon [20]. Significantly higher values of breaking strength at low

TABLE III. Physical properties of silicon and sapphire at 20 K and metals at 2 K. Some of the indicated references comprise temperature dependencies, which are included in the STN model presented in Secs. VI and VII.

	Silicon	Sapphire	Ti6Al4V	Titanium	Al5056[a]
T (K)	20	20	2.0	2.0	2.0
ϕ_{bulk} (-)	1×10^{-9} [23][b]	3×10^{-9} [24]	1×10^{-4} [25][c]	1×10^{-6} [26]	2.5×10^{-8} [27]
σ_y (MPa)	230 [28][d]	400 [20][d]	1600 [29]	1200 [29]	280 [29]
$\lambda(T)$ (W/m/K)	4940 [30]	6000 [31]	0.22 [32]	2.5 [32]	2.0 [33]
$c_p(T)$ (J/kg/K)	3.40 [34]	0.69 [35]	0.01 [32]	0.12 [32]	0.10 [36]
$\alpha(T)$ (1/K)	-2.9×10^{-9} [37]	1.3×10^{-8} [38]	6.0×10^{-6} [39]	5.5×10^{-8} [39]	14×10^{-6} [29]
β (1/K)	-7.9×10^{-6} [40][e]	-4.4×10^{-6} [41][e]	-4.6×10^{-4} [42][e]	-4.6×10^{-4} [42][e]	1.2×10^{-4} [43]
E (GPa)	130 [44][f]	360 [45][f]	127 [46][f]	130 [29]	81 [43]
ρ (kg/m^3)	2330 [47]	3980 [47]	4540 [32]	4540 [32]	2660 [32]
α_{surf} (m)	5×10^{-13} [48]	5×10^{-13} [g]	0.0	0.0	0.0

[a]Physical properties, except for ϕ_{bulk}, λ and c_p, are taken from Al5083 due to the lack of data at cryogenic temperatures for Al5056.
[b]Value given at $T = 10$ K and applied in accordance with the silicon surface loss parameter reported in [48].
[c]Value given at $T = 80$ K due to lack of data at lower temperatures.
[d]For brittle materials, the yield strength σ_y and the ultimate strength σ_{max} are nearly equivalent. The data given for 300 K tend to increase by about 10% at cryogenic temperatures.
[e]Values in the range of 80 K to 300 K; expected to decrease further at cryogenic temperatures.
[f]Data given for 300 K tend to increase by about 30% at cryogenic temperatures.
[g]For sapphire, the same surface loss parameter as silicon is assumed due to the lack of experimental data.

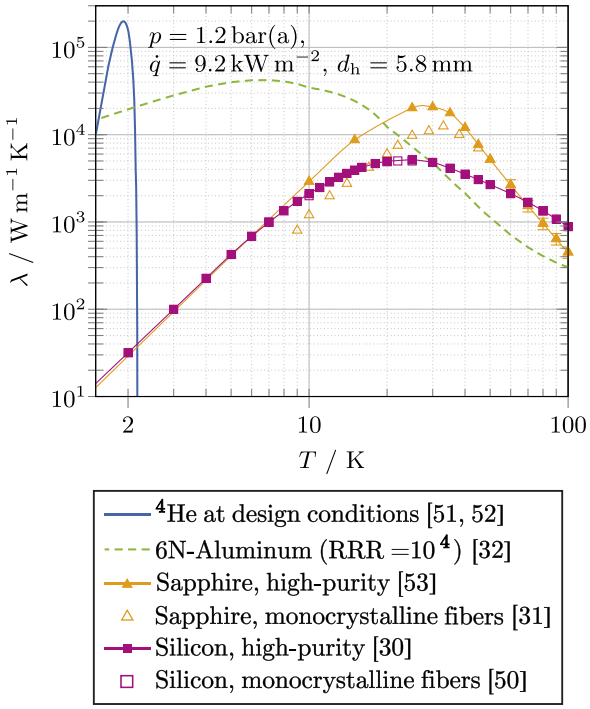

FIG. 5. Thermal conductivity of helium compared to several high-purity solids [30–32,50–53].

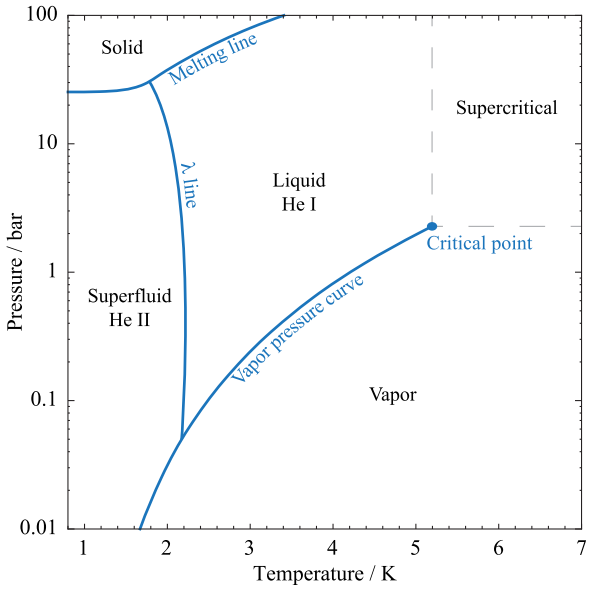

FIG. 6. Phase diagram of ^{4}He.

temperatures, spread in the range of 1000 MPa to 2600 MPa, have been recently measured [21] and certified using samples produced in Japan by Shinkosha [22] and machined from a single ingot.

C. Thermal behavior

The thermal behavior depends on the thermal conductivity in the range of 10 K to 30 K. In thin suspension fibers, the phonon boundary scattering may significantly reduce the bulk conductivity [49]. Thermal conductivity data for high-purity monocrystals and monocrystalline fibers of silicon and sapphire are therefore compared in Fig. 5. In silicon fibers, a marginal reduction of thermal conductivity is visible [50], whereas a significant reduction is reported for sapphire fibers [31]. Further thermal conductivity measurements of silicon and sapphire fiber samples are planned within future R&D activities.

The nominal heat load from Eq. (1) together with the dimensions in Table II and the thermal conductivity data of monocrystalline fibers according to Fig. 5 yield temperature gradients along the marionette suspension of $\Delta T_\mathrm{ma} = 3$ K for silicon and $\Delta T_\mathrm{ma} = 5$ K for sapphire.

IV. CONCEPT WITH He-II–FILLED MARIONETTE SUSPENSION TUBE

A. Motivation for using He-II

Cryogenic fluids have been extensively used to operate the second generation of resonant GW detectors [54], and later have been proposed for cooling the test masses of the GW interferometers [55]. The use of He-II is motivated by the exceptional properties of superfluid helium, rather than its temperature around 2 K. The abundant ^{4}He isotope can exist in two liquid forms, separated by the λ line depicted in Fig. 6. While liquid helium at $T > T_\lambda$ (called He-I) exhibits normal fluid behavior, it becomes a quantum fluid (called He-II) at $T < T_\lambda$ when fractions of the atoms condense in the ground state as a Bose-Einstein condensate [56,57]. The He-II is composed of a normal and a superfluid component, as described by the two-fluid model [58,59]. The second-order phase transition from He-I to He-II is associated with dramatic property changes. Particularly relevant is the exceptional increase in thermal conductivity, yielding a thermal reservoir to absorb and conduct heat in the quietest possible manner. This property enables the concept of heat extraction from the ET-LF payload via a static He-II column inside a thin-wall marionette suspension tube. For the conditions given in Fig. 5, He-II can exceed the thermal conductivity of high-purity sapphire or silicon by at least 1 order of magnitude. This concept provides a temperature of 2 K at the marionette, which is an essential parameter to reduce the STN, as discussed in Sec. VI.

Related to the thermal conductivity, the quantum fluid properties may imply that thermal and mechanical dissipation in the static He-II column is very low, and that momentum transfer to/from the suspension tube may not take place due to superfluidity. These hypotheses, however, require experimental validation, as the integration of a quantum fluid in suspensions of GW detectors has never been analyzed and presents a new field of research.

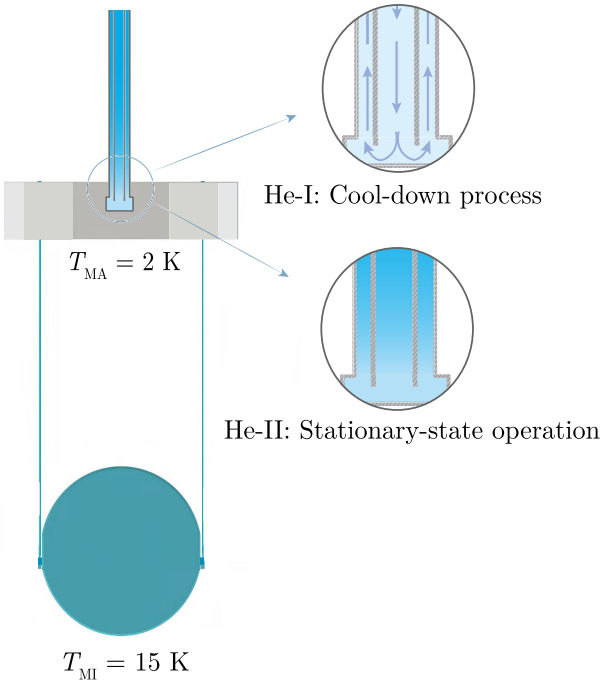

FIG. 7. Conceptual layout of the He-II marionette suspension.

B. Conceptual layout

The conceptual layout of the He-II marionette suspension is depicted in Fig. 7. In addition to the thin-wall marionette suspension tube, an internal guiding tube enables cooldown of the payload in counterflow with supercritical helium ($p > 2.3$ bar) at adjustable supply temperatures. The helium supply can be implemented at a cooling interface on the PF, using multiple thin-wall and "soft" capillaries attached to vibration isolation systems, similar to the heat link concept in KAGRA [15,60]. The capillaries connect the cooling interface to a cryogenic supply unit in the vicinity of the cryostat, cf. [61,62]. Exemplary capillary dimensions are given in [63].

For steady-state operation, the normal He-I is transformed in a static He-II column [61]. The internal guiding tube has no function in this case—i.e., heat conduction takes place via the entire He-II cross section. By contact with the He-II suspension, the marionette reaches a temperature of 2 K. The silicon mirror temperature is around 15 K due to the heat load and the temperature gradient in the monocrystalline mirror suspensions.

C. Mechanical dimensioning

The marionette suspension tube carries the mechanical load of the MA and the MI. The dimensioning includes a mechanical safety factor SF = 3 with regard to the yield strength σ_y of the tube material (cf. Table III for material options). Besides low-temperature ductility and mechanical strength, a decisive constraint in the material choice is related to suspension losses. This yields a preference for titanium, as discussed in Sec. VI.

D. Thermal dimensioning

In this marionette suspension concept, the thermal dimensioning (i.e., the He-II cross section) is independent from the mechanical dimensioning (i.e., the suspension tube wall cross section). The two-fluid model [58,59] describes the heat transport in static He-II by a counterflow between the normal and the superfluid components on a molecular level—i.e., there is no macroscopic movement of the bulk liquid. The most efficient laminar regime is achieved only in narrow channels of $d < 10$ μm, where the normal and superfluid components do not interact. In channels of $d > 1$ mm, an additional turbulent term starts dominating the temperature gradient by the excitation of rotons and a resulting mutual friction among the two components. The mutual friction signifies a dissipative process that limits the heat transport [56], but the thermal conductivity remains nonetheless higher than in pure solids, as shown in Fig. 5.

The temperature gradient along the He-II column in the marionette suspension is given by

$$\Delta T_{\mathrm{ma}} = \frac{32\eta L_{\mathrm{ma}}}{(d_{\mathrm{h}}\rho s)^2 T}\dot{q} + \frac{L_{\mathrm{ma}}}{h\left(\frac{T}{T_\lambda}\right) g_{\mathrm{peak}}(p)}\dot{q}^{3.4}, \qquad (2)$$

where the left term signifies the analytic description of the laminar regime [57] and the right term uses the model from Sato *et al.* [51] for the turbulent regime. L_{ma} denotes the marionette suspension length, η the dynamic viscosity, ρ the density and s the entropy of the He-II, d_{h} refers to the hydraulic diameters of the circular and the annular cross sections shown in Fig. 8, $\dot{q}$ is the heat flux, and $h(T)$ and $g_{\mathrm{peak}}(p)$ are empirical functions from Sato *et al.* [51]. For the baseline design under nominal operating

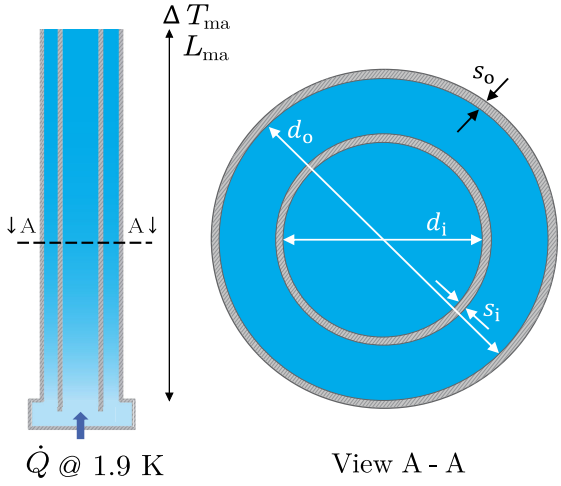

FIG. 8. Suspension tube design.

TABLE IV. Suspension tube design parameters.

Parameter	Value
L_{ma}	1.0 m
M_{MA}	200 kg
M_{MI}	200 kg
Constraints:	
Mechanical SF	3.0
$T(y = L_{ma})$	1.9 K
$p_{He\text{-}II,in}$	1.2 bar(a)
ΔT_{ma}	50 mK
$\dot{Q}$	0.5 W
Design results:	
d_o	8.30 mm
s_o	0.36 mm
d_i	5.80 mm
s_i	0.05 mm

conditions, the contribution from the laminar term is negligibly small.

Defining a temperature gradient of $\Delta T_{ma} = 50$ mK with regard to the overall He-II operating concept explained in [61], the suspension tube design parameters are summarized in Table IV. The suspension tube lower end temperature is the highest temperature in the He-II system set to 1.9 K, where the thermal conductivity peak is located. The suspension tube outer diameter d_o results from the required He-II cross section, whereas the wall thickness s_o results from the mechanical design. The inner guiding tube dimensions are chosen such that equal cross sections of the inner tube and the annular gap yield similar flow velocities during cooldown. Figure 9 shows the relation between the required suspension tube diameter d_o and the heat load that can be extracted at $\Delta T_{ma} = 50$ mK and $L_{ma} = 1$ m.

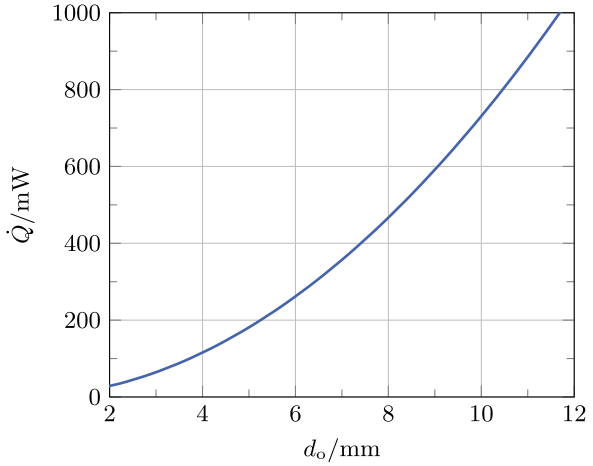

FIG. 9. Cooling capacity of the He-II suspension as a function of the outer tube diameter.

E. Cooldown with normal He-I flow

One main advantage of this concept is the ability for convective cooldown of the ET-LF payload. This is enabled by normal He-I flow through the double-walled marionette suspension tube, as indicated in Fig. 7. The heat flux $\dot{q}$ from the marionette to the helium flow is correlated by

$$\dot{q} = \alpha(T_{wall} - T_{He}), \tag{3}$$

where α denotes the heat transfer coefficient, T_{wall} the wall temperature, and T_{He} the fluid temperature. Using aluminum alloy 1200 as marionette material, the marionette temperature change is given by

$$\frac{dT_{MA}(t)}{dt} = \frac{-\dot{q}A_{HT}}{c_{p,Al}(T_{MA}(t))M_{MA}}, \tag{4}$$

where A_{HT} is the heat transfer area, $c_{p,Al}(T)$ the specific heat capacity, and M_{MA} the marionette mass. This equation simplifies the marionette as a block capacitance, neglecting the influences of finite heat conductivity. The cooldown process is therefore analyzed numerically by CFD simulation. In the model development process, simulations were set up in ANSYS Fluent® (finite volume method) and in COMSOL Multiphysics® (finite element method), allowing validation of the numerical model independence.

Simulations are carried out for the marionette and suspension design parameters in Tables II and IV. The suspension tube length is 1.105 m in total, of which 105 mm are centrally connected to the bottom half of the marionette, passing through a slightly wider bore in the upper half. This insertion yields a heat transfer area of $A_{HT} \approx 2750$ mm^2. Table V lists additional simulation parameters and material properties in the relevant temperature range of 3.0 K to 293.15 K. The 3 K denotes the

TABLE V. CFD simulation parameters and material properties of the marionette convective cooling model.

Parameter/property	Value/expression
$\dot{M}_{He}$	1.0 g s^{-1}
$p_{He,out}$	2.5 bar(a)
$T_{He,in}(t)$	$\max\{\bar{T}_{MA}(t) - \Delta T_{MA\text{-}He,in}, 3.0\ \text{K}\}$
$\Delta T_{MA\text{-}He,in}$	100 K
$T_{MA}(t = 0)$	293.15 K
$\bar{T}_{MA}(t_{end})$	3.01 K
d_{MA}	700 mm
h_{MA}	210 mm
A_{HT}	2750 mm^2
$\lambda_{Al}(T)$	59.4…502 W m^{-1} K^{-1} [64]
$c_{p,Al}(T)$	0.29…942 J kg^{-1} K^{-1} [32]
$\lambda_{Ti}(T)$	4.03…36.0 W m^{-1} K^{-1} [32]
$c_{p,Ti}(T)$	0.20…520 J kg^{-1} K^{-1} [32]

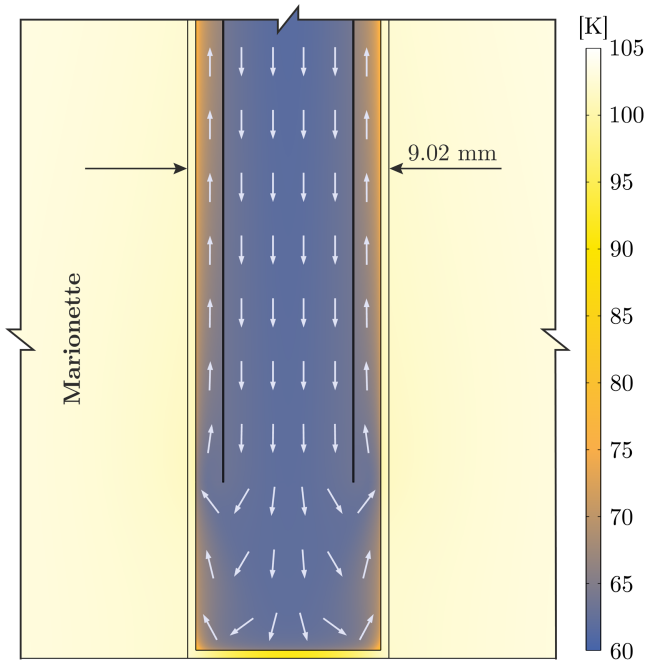

FIG. 10. Temperature contours and velocity field in the bottom section of the marionette; intermediate results at $\bar{T}_{\mathrm{MA}} \approx 103$ K.

convective precooling limit before the transformation to He-II operation.

In the numerical model, the geometry is simplified by axial symmetry, yielding a cylindrical marionette instead of the octagonal prism shape displayed in Fig. 2. The helium properties are implemented via REFPROP [65] in ANSYS Fluent®, and by the Peng-Robinson (Twu) equation of state [66] in COMSOL Multiphysics®. The operating conditions in Table V yield exclusively turbulent flow regimes. In order to solve the flow problems, the standard turbulence eddy viscosity $\mathrm{k}-\epsilon$ model with renormalization group (RNG) methods developed by Yakhot *et al.* [67] is applied for its accuracy regarding heat transfer [68]. Scalable wall functions are implemented for the generated spatial discretization, since they enable an adequate resolution of thermally and fluid-dynamically induced effects close to the walls within the fluid domain.

The helium supply temperature $T_{\mathrm{He,in}}$ is set as a function of the average marionette temperature for controlled cooldown. A constant $\Delta T = 100\ \mathrm{K} = \bar{T}_{\mathrm{MA}}(t) - T_{\mathrm{He,in}}$ is defined until the lowest helium supply temperature of 3 K is reached and held constant subsequently. The low-pressure limit of $p_{\mathrm{He,out}} = 2.5$ bar(a) ensures supercritical single-phase flow during the entire cooldown process. The marionette and suspension tube surfaces are considered adiabatic, while the internal guiding tube is diabatic.

Figure 10 shows exemplary results of the CFD simulation at an intermediate time step with $\bar{T}_{\mathrm{MA}} = 103$ K and $T_{\mathrm{He,in}} = 3$ K. At the bottom end, the helium flow is returned from the inner guiding tube to the outer annular gap. Due to internal heat exchange in the suspension,

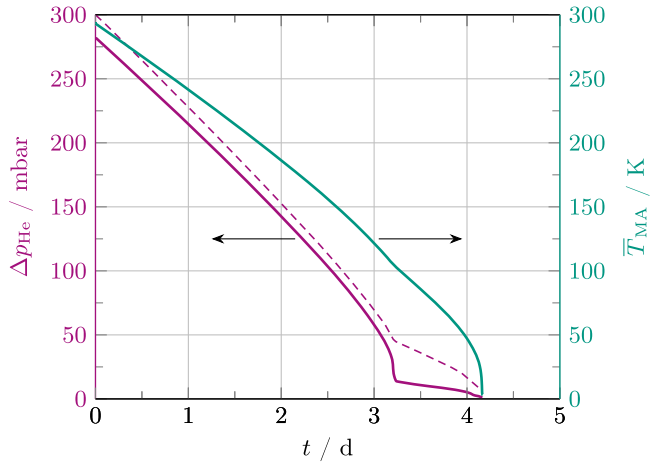

FIG. 11. Helium pressure loss in the suspension tube and marionette temperature during cooldown for the conditions listed in Table V.

the helium supply flow is heated up by $\Delta T \approx 57$ K before entering the marionette heat transfer area A_{HT} at $T_{\mathrm{He}} \approx 60$ K. Yet, the temperature difference between marionette and helium is still around 40 K, driving the heat extraction from the marionette. In comparison, the temperature gradients within the marionette are small due to the high thermal conductivity of aluminum alloy 1200, especially at $T < 100$ K [64].

Results of the numerical simulation in terms of cooldown time and pressure loss are presented in Fig. 11. The pressure loss $\Delta p_{\mathrm{He}} = p_{\mathrm{He,in}} - p_{\mathrm{He,out}}$ decreases with temperature due to decreasing flow velocities at increasing densities. A distinct point in the cooldown curve is found at $t \approx 3.2$ d, where $T_{\mathrm{He,in}}$ reaches the low-temperature limit of 3 K. Toward the end of the cooldown at $t \geq 4$ d and $T \leq 50$ K, the marionette temperature decreases rapidly due to the T^3 dependence of specific heat capacity. The results in Fig. 11 indicate that the marionette can be cooled from ambient to operating temperature in about 4.2 d. With a helium mass flow rate of 1 $\mathrm{g\,s^{-1}}$, the pressure drop in the suspension is $\Delta p_{\mathrm{He}} < 300$ mbar, which is compatible with the helium supply system presented in [61]. In addition to the numerical approach, the results are verified by implementing heat transfer and pressure drop correlations in a set of differential equations, yielding the dashed line for the pressure drop in Fig. 11. A more detailed discussion of this model exceeds the scope of this paper.

In a next step, the cooldown of a silicon test mass is investigated, using the data of the marionette cooldown model to define the temperatures of the mirror suspensions at their upper ends. Radiative heat transfer is included in this model, as former studies have shown the need of combined convective and radiative cooling to achieve sufficient cooldown rates [62]. The simulation data are summarized in Table VI. Conservative assumptions are made for the emissivity of silicon with $\epsilon_{\mathrm{MI,Si}} = 0$ at

TABLE VI. Simulation parameters used in the test mass cooldown model.

Parameter	Value
M_{MI}	200 kg
d_{MI}	450 mm
h_{MI}	570 mm
d_{mi}	3.0 mm
L_{mi}	1.2 m
T_{Shield}	5.0 K
$\epsilon_{\mathrm{MI,Si}}(T)$	0.41…0.75 [69][a]
$\lambda_{\mathrm{Si}}(T)$	2330…5130 $\mathrm{W\,m^{-1}\,K^{-1}}$ [30]
$c_{\mathrm{p,Si}}(T)$	0.28…707 $\mathrm{J\,kg^{-1}\,K^{-1}}$ [70]

[a]Range represents values from 120 K to 260 K for a sample with dimensions 70 mm × 30 mm × 103.5 mm.

$T < 120$ K and $\epsilon_{\mathrm{MI,Si}} = 0.75$ at $T > 260$ K, due to the lack of data. Thermal radiation is implemented from the test mass to a surrounding black body at $T = 5$ K starting at $t = 0$, representing the thermal shield operation around the payload [61].

Figure 12 contains the simulation results, showing that the silicon test mass can be cooled from ambient to operating temperature in about 12.8 d. The first phase at $t < 5.2$ d is driven by thermal radiation, where temperature differences between the test mass and the shield are large, and the marionette cooldown is yet in progress. In the second phase, thermal radiation is effectively disabled with $\epsilon_{\mathrm{MI,Si}} = 0$. The heat extraction from the test mass occurs exclusively via the test mass suspension fibers to the helium-cooled marionette. Toward the cooldown end, this mechanism is amplified by increasing thermal conductivity values of silicon and the strongly decreasing heat capacity.

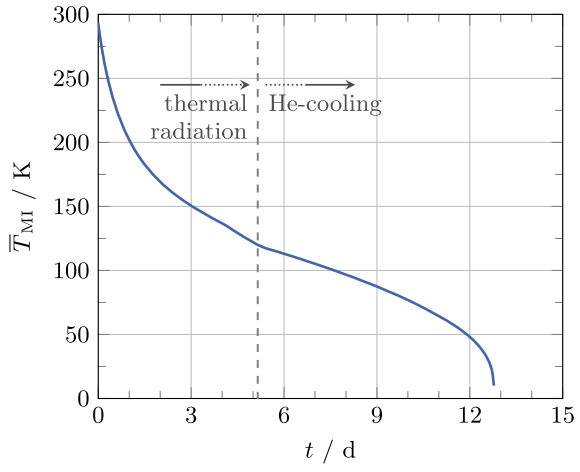

FIG. 12. Cooldown of an ET-LF silicon test mass installed within a thermal shield at $T = 5$ K for the conditions listed in Tables V and VI.

V. MODELING OF SUSPENSION THERMAL NOISE

A. Theoretical foundations

Thermal noise is a thermally driven motion, which is directly related to the mechanical dissipative behavior of a system. Since thermal noise is a generalized type of Brownian motion with a random displacement of particles, it can be described using the fluctuation-dissipation theorem (FDT) [71]. It states that the dissipations in the system are the driving force for thermal fluctuations, which are presented in the form of a displacement spectral density. The FDT is able to include the contributions of various dissipative sources, using an equivalent macroscopic mechanical model that describes the total impedance of the system in the frequency domain [72]. The theoretical foundations and further details of thermal noise modeling in mechanical systems, especially for suspensions used in gravitational wave detectors, are explained in [12,72–76]. The general approach can be summarized by the following steps:

(1) Choice of the representative mechanical model and the dissipation mechanisms affecting the system.
(2) Definition of the one-dimensional equation of motion for the mechanical displacement $x(t)$ and its Fourier transform $X(\omega)$.
(3) Definition of the mechanical impedance $Z(\omega)$ and its inverse, the admittance $Y(\omega)$. $Z(\omega)$ is the ratio between the Fourier transforms of the applied force and system velocity and is calculated by applying an external force on the system and inspecting its reaction based on its equation of motion:

$$Z(\omega) \equiv \frac{F}{i\omega X(\omega)} \quad \text{and} \quad Y(\omega) \equiv [Z(\omega)]^{-1}. \tag{5}$$

(4) Calculation of the thermal noise spectral density based on the FDT:

$$S_{\mathrm{xx}}(\omega) = \frac{4k_{\mathrm{B}}T}{\omega^2} \cdot \mathrm{Re}([Z(\omega)]^{-1}), \tag{6}$$

where k_{B} is the Boltzmann constant, T the suspension temperature, and ω the angular frequency.

B. Dissipation in a pendulum system

Energy dissipation in a mechanical system can arise from various sources, contributing directly to the generation of thermal noise [12]. The dissipation is quantified by the loss angle ϕ, representing the ratio between the imaginary and the real restoring force in the system [77].

The suspension thermal noise model in this paper considers the ET-LF payload as a double pendulum, with MA and MI as point masses and suspensions with homogeneous mechanical losses. The loss angle of a

suspension includes the summation of different dissipation mechanisms as

$$\phi_{\mathrm{susp}}(\omega) = \phi_{\mathrm{bulk}} + \phi_{\mathrm{therm}}(\omega) + \phi_{\mathrm{surf}} + \phi_{\mathrm{join}}. \quad (7)$$

Bulk losses, ϕ_{bulk}, designate intrinsic dissipations in the bulk material. These losses arise from the structural composition and from defects in the material, depending on temperature and frequency [13]. The frequency dependence is usually considered negligible, and the temperature dependence is determined experimentally [78]. For the ET-LF marionette suspension, several materials are proposed as depicted in Tables II and III. Their bulk losses at cryogenic temperatures are summarized in Table VII. For the mirror suspensions, the proposed materials include monocrystalline silicon or sapphire. The bulk loss angles applied in this STN model are summarized in Table III.

Thermoelastic losses, ϕ_{therm}, are frequency-dependent losses occurring in a suspension under tension, characterized by a broad maximum at a characteristic frequency [12,86]. These losses originate from local temperature gradients generated by the compression and expansion at the suspension bending point. These gradients induce a heat flux that is accompanied with entropy generation (i.e., energy dissipation) [48,87]. For modeling, [87] proposes to consider both a contribution from the linear expansion coefficient α, and a nonlinear contribution from the temperature dependence of the Young's modulus E via the thermal elastic coefficient $\beta = \mathrm{d}\ln E/\mathrm{d}T$:

$$\phi_{\mathrm{therm}}(\omega) = \frac{ET}{\rho c_{\mathrm{p}}}\left(\alpha - \sigma\frac{\beta}{E}\right)^2\left(\frac{\omega\tau}{1+(\omega\tau)^2}\right), \quad (8)$$

with σ as the suspension tension and τ as the thermal diffusion time, for a circular suspension given as [88]

$$\tau = \frac{d^2\rho c_{\mathrm{p}}}{13.55\lambda}, \quad (9)$$

with d as the suspension diameter and λ as the thermal conductivity of the suspension material. This type of loss depends on geometry and tension [cf. Eq. (8)]. Thus, a reduction or nullification via an optimized suspension profile design, as applied in silica suspensions in current detectors, could be possible [28].

Surface losses, ϕ_{surf}, are mechanical losses in a thin surface layer h_{s}, the dissipation depth, which differ from the bulk losses [48,89]. These depend on the surface quality and on treatment techniques (e.g., polishing, dry or wet chemical etching) but are generally not yet fully understood [80]. ϕ_{surf} are determined from experimental data, using the surface loss parameter $\alpha_{\mathrm{surf}} = h_{\mathrm{s}}\phi_{\mathrm{bulk}}$. The relation between ϕ_{surf}, α_{surf}, the geometry factor μ, the surface area A_{surf} and the volume V is given by [89] and simplified for thin circular fibers with $\mu = 2$ to

$$\phi_{\mathrm{surf}} = \alpha_{\mathrm{surf}}\frac{\mu A_{\mathrm{surf}}}{V} = h_{\mathrm{s}}\phi_{\mathrm{bulk}}\frac{8}{d}. \quad (10)$$

This equation shows that surface losses become increasingly relevant with higher surface-to-volume ratio.

Jointing losses, ϕ_{join}, are additional mechanical losses resulting from the clamping between the suspensions and their anchors. The minimization of these losses requires dedicated numerical simulations including the real payload geometry alongside experimental validation [90]. Equivalently to the ET conceptual design study [2] and the design report update [5], this type of loss requires a more advanced design and is hence not yet considered in the model.

TABLE VII. Bulk loss angles ϕ_{bulk} of various materials at cryogenic temperatures.

Material	Type/treatment	T (K)	ϕ_{bulk} (-)
Silicon	Single crystal (100) [23]	3.5	5×10^{-10}
		10	1×10^{-9}
		20	3×10^{-9}
Silicon	Single crystal (100) [11]	10	5×10^{-9}
		20	8×10^{-9}
Silicon	Single crystal (100) [79]	18	5×10^{-9}
Silicon	Single crystal (111) [11]	10	1.1×10^{-8}
		20	1.2×10^{-8}
Sapphire	Single crystal, annealed [24]	10	2×10^{-9}
		20	3×10^{-9}
Sapphire	Single crystal, annealed [80]	4.0	2×10^{-10}
		10	1×10^{-9}
		20	3×10^{-9}
Sapphire	Hemlite grade [81]	4.2	4×10^{-9}
		10	5×10^{-9}
		20	5.6×10^{-9}
Titanium	Grade 1, annealed [26]	1...20	6×10^{-7}
Titanium	Grade 1, stress-relieved [26]	1...20	1×10^{-6}
Titanium	Grade 1, untreated [26]	1...20	1×10^{-6}
Titanium	Grade 2 [82]	4.2	5×10^{-7}
		20	1×10^{-6}
Ti6Al4V	Grade 5 [25]	80	1×10^{-4}
Al5056	Untreated [83]	2.0	6×10^{-8}
Al5056	Annealed [83,84]	2.0	2.5×10^{-8}
Al5056	⋯ [85]	2.0	1.6×10^{-7}

C. Dynamic behavior of the pendulum system

The suspension thermal noise modeling requires the mechanical impedance $Z(\omega)$ of the payload derived from the equations of motion as given in Eq. (6). The double pendulum system representing the ET-LF payload is depicted in Fig. 13. It is modeled as a double mode oscillator with a stiffness constant for each pendulum stage [12,76]. The equations of motion in the frequency domain are given as

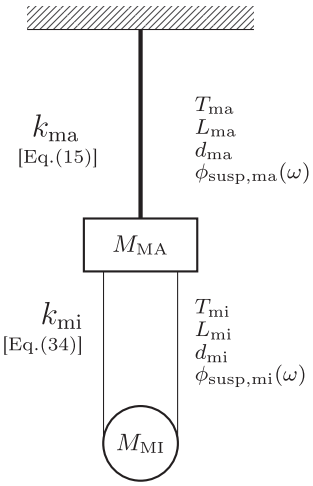

FIG. 13. Scheme of the representative mechanical system used to model the STN of the ET-LF payload (ma = marionette suspension, MA = marionette, mi = mirror suspension, MI = mirror).

$$0 = -M_{\mathrm{MA}}\omega^2 X_{\mathrm{ma}} + k_{\mathrm{ma}} X_{\mathrm{ma}} + k_{\mathrm{mi}}(X_{\mathrm{ma}} - X_{\mathrm{mi}}), \quad (11)$$

$$F = -M_{\mathrm{MI}}\omega^2 X_{\mathrm{mi}} + k_{\mathrm{mi}}(X_{\mathrm{mi}} - X_{\mathrm{ma}}), \quad (12)$$

where F is an external force applied onto the mirror stage. The spring constants k_{ma} and k_{mi} of the marionette and the mirror stages, respectively, are calculated via the representative mechanical system of each pendulum stage. González [75] provides a detailed summary of mechanical models applicable to suspensions used in gravitational wave detectors.

The *marionette stage* is modeled using a simple pendulum with a suspended point mass, considering a lossless gravitational potential and a lossy elastic potential as the only energy sources. The latter is a simplified treatment to introduce dissipation, given that the violin modes of the marionette suspension have been shown to have a negligible impact compared to the dominating ones of the mirror suspensions. Hence, the marionette violin modes do not need to be considered in the dynamics of the representative system. The marionette spring constant k_{ma} is obtained from the lossless gravitational spring constant k_{g} and the lossy elastic spring constant k_{el} via

$$k_{\mathrm{ma}} = k_{\mathrm{g}} + k_{\mathrm{el}}(1 + i\phi_{\mathrm{susp}}(\omega)). \quad (13)$$

Introducing the dilution factor D, which depicts the ratio between the system's elastic and gravitational potential energies [12,77], as

$$D = \frac{k_{\mathrm{el}}}{k_{\mathrm{g}}} = \frac{n\sqrt{EI\sigma}}{2L^2}\frac{L}{Mg} = \frac{1}{2L}\sqrt{\frac{nEI}{Mg}}, \quad (14)$$

with M as the total mass suspended by n wires, σ as the tension in each wire, I as the area moment of inertia, g as the gravitational acceleration, and L as the suspension length, k_{ma} yields [91]

$$k_{\mathrm{ma}} = k_{\mathrm{g}}(1 + D + i\phi_{\mathrm{pend}}(\omega)). \quad (15)$$

The definition of the pendulum loss angle $\phi_{\mathrm{pend}}(\omega)$ in Eq. (16) shows that the pendulum losses are lower than the suspension losses ϕ_{susp} according to Eq. (7) due to dilution via D:

$$\phi_{\mathrm{pend}}(\omega) = \phi_{\mathrm{susp}}(\omega)D. \quad (16)$$

The equation of motion for the marionette stage includes only a complex spring potential

$$-k_{\mathrm{ma}}x(t) = M_{\mathrm{MA}}\frac{\partial^2 x(t)}{\partial t^2}, \quad (17)$$

yielding in the frequency domain $[x(t) \to X(\omega)\cdot e^{i\omega t}]$

$$k_{\mathrm{ma}}X(\omega) - M_{\mathrm{MA}}\omega^2 X(\omega) = 0. \quad (18)$$

The *mirror stage* is modeled using a pendulum consisting of four anelastic suspension fibers suspending a point mass. Thus, in addition to the pendulum's degree of freedom (d.o.f.), from which the pendulum mode is extracted, the degrees of freedom related to the transverse motion along the suspension are also included in order to obtain the infinite series of violin modes associated with its bending [74,75,91].

The effective mirror spring constant k_{mi} associated with the suspension elasticity and gravitational restoring force is derived by solving the elastic equation for a slightly deflected suspension stretched by a tension σ [75,91]:

$$-E_{\mathrm{cx}}I\frac{\partial^4 x(y,t)}{\partial y^4} + \sigma\frac{\partial^2 x(y,t)}{\partial y^2} = \rho S\frac{\partial^2 x(y,t)}{\partial t^2}. \quad (19)$$

The introduction of the Fourier transform of the displacement $X(y,\omega)$ yields

$$E_{\mathrm{cx}}I\frac{\partial^4 X(y,\omega)}{\partial y^4} - \sigma\frac{\partial^2 X(y,\omega)}{\partial y^2} - \rho S\omega^2 X(y,\omega) = 0, \quad (20)$$

with S as the cross-sectional area of the suspension. The complex Young's modulus E_{cx} introduces the dissipation into the system as

$$E_{\mathrm{cx}} = E(1 + i\phi_{\mathrm{susp}}(\omega)). \quad (21)$$

The general solution of Eq. (20) yields the displacement of the suspension $X(y,\omega)$ along the suspension axis y:

$$X(y,\omega) = C_1\sin(k_{\mathrm{s}}y) + C_2\cos(k_{\mathrm{s}}y) + C_3e^{k_{\mathrm{e}}y} + C_4e^{-k_{\mathrm{e}}y}, \quad (22)$$

with k_s as the wave number associated with the flexural stiffness of the suspension [74,92]

$$k_s = \sqrt{\frac{\sigma + \sqrt{\sigma^2 + 4E_{cx}I\rho S\omega^2}}{2E_{cx}I}}, \tag{23}$$

and k_e as the wave number of an elastic fiber

$$k_e = \sqrt{\frac{-\sigma + \sqrt{\sigma^2 + 4E_{cx}I\rho S\omega^2}}{2E_{cx}I}}, \tag{24}$$

where the constants C_1 to C_4 are defined from the system boundary conditions. For simplicity, henceforth the frequency dependency of $X(y,\omega)$ is dropped.

The first two boundary conditions result from the upper part of the suspension at $y = 0$, where the fixed clamping on the marionette yields

$$X(0) = 0 \quad \text{and} \quad \frac{\partial X}{\partial y}(0) = 0. \tag{25}$$

The third and the fourth boundary conditions are associated with the bottom part at $y = L_{mi}$, where the mirror is attached and foregoes a displacement of X_0:

$$X(L_{mi}) = X_0, \tag{26}$$

$$\frac{\partial X}{\partial y}(L_{mi}) = 0 \quad \text{or} \quad \frac{\partial^2 X}{\partial y^2}(L_{mi}) = 0. \tag{27}$$

Assuming the mirror as a lumped mass causes the suspension slope at the bottom to be a free parameter [75], Somiya [92] reports how this boundary condition can be defined for different mirror positioning approaches. In the case of the mirror facing in the beam direction, the suspension bends at the attachment point, yielding $\frac{\partial X}{\partial y}(L_{mi}) = 0$ [91]. This condition is applied in this paper, equivalently to the ET-LF design in [5].

After defining the suspension displacement function $X(y)$ according to Eq. (22), the effective mirror spring constant k_{mi} can be derived by applying an external force F on the suspended mass at $y = L_{mi}$ [74,91]. From the equation of motion of a lumped mass

$$E_{cx}I\frac{\partial^3 X}{\partial y^3}(L_{mi}) - \sigma\frac{\partial X}{\partial y}(L_{mi}) - M_{MI}\omega^2 X(L_{mi}) = F, \tag{28}$$

with $\frac{\partial X}{\partial y}(L_{mi}) = 0$ as a boundary condition, the mirror spring constant k_{mi} for four suspensions is given by Eq. (34).

The mechanical impedance $Z_{horz}(\omega)$, needed for the STN calculation in Eq. (6), is defined by the equations of motion for the double pendulum system, presented in matrix form in Eq. (35). Through this motion matrix, the mechanical impedance $Z_{horz}(\omega)$ is obtained from Eq. (36). The spring constants k_{ma} and k_{mi} implemented in our STN model are taken from Eqs. (15) and (34).

The system dynamics described above refer to the horizontal d.o.f., representing the dominant source for the STN. Nonetheless, the vertical d.o.f. delivers also a non-negligible contribution to the STN and is included in the model. The approach for modeling the vertical impedance $Z_{vert}(\omega)$ is analogous to the algorithm above, whereby both the marionette and mirror stages are represented via simple pendulum systems, whose vertical spring constants are given by [91]

$$k_{mi,vert} = \frac{4E_{mi}S_{mi}}{L_{mi}}(1 + i\phi_{susp,mi}), \tag{29}$$

$$k_{ma,vert} = (2\pi \cdot 0.4\ \text{Hz})^2 M_{MA+MI}(1 + i\phi_{susp,ma}). \tag{30}$$

The vertical spring constant for the marionette suspension can be evaluated as a set of two springs connected in series, namely the marionette suspension itself and the spring blades at its upper part. The resulting vertical spring constant is dominated by the soft magnetic spring blades of the superattenuator system. The value 0.4 Hz in Eq. (30) refers to the natural frequency measured for the magnetic antispring blades in AdVirgo [91]. Similar spring blades are assumed in this model for ET-LF.

Finally, the overall STN spectral density is

$$S_{xx}^{total}(\omega) = S_{xx}^{horz}(\omega) + \theta_{vh}^2 S_{xx}^{vert}(\omega), \tag{31}$$

where θ_{vh} is the vertical-to-horizontal coupling factor. Weak coupling of vertical motion to horizontal motion results from the nonparallel alignment of the test masses at the ends of the interferometer arms due to the Earth's curvature. For a 10 km ET-LF arm, θ_{vh} yields

$$\theta_{vh} = \frac{L_{arm}}{d_{Earth}} = 7.8 \times 10^{-4}. \tag{32}$$

D. Implementation of temperature distribution

For systems including nonuniform temperatures, the STN is usually modeled using the normal modal approach [2,5,91], as the standard FDT assumes a single homogeneous temperature in the whole system, as seen in Eq. (6). The modal approach can be a heavy computational task [93] and includes only homogeneous dissipation. To include inhomogeneous losses, Levin [73] introduces an extended formulation of the standard FDT. Komori *et al.* [94] propose a discrete version of this extended FDT, which can be applied for STN modeling of systems with inhomogeneous temperatures, such as cryogenic payloads. This approach foresees the discretization of the system into elements, where each element is associated with a

homogeneous temperature and an individual mechanical impedance, where the thermal noise spectral density sensed by the element j of the system is given by [94]

$$S_{xx}(\omega) = \frac{2k_B}{\omega^2}\sum_j T_j Z^{-1}(Z_j + Z_j^{\dagger})Z^{-1\dagger}. \tag{33}$$

The STN model in this paper uses the discrete FDT approach for modeling the cryogenic payload consisting of two elements (i.e., mirror stage and marionette stage). Here homogeneous losses and a constant temperature along the suspensions, namely the highest temperatures at the lower ends, are assumed.

$$k_{mi} = \frac{-E_{cx} I \frac{\partial^3 X}{\partial y^3}(L_{mi})}{X(L_{mi})} = \frac{4E_{cx} I k_s k_e (k_s^3 \cos(k_e L_{mi}) + k_s^2 k_e \sin(k_e L_{mi}) + k_e^3 \sin(k_e L_{mi}))}{(k_s^2 - k_e^2)\sin(k_e L_{mi}) - 2k_s k_e \cos(k_e L_{mi})}, \tag{34}$$

$$\begin{bmatrix} k_{ma} + k_{mi} - M_{MA}\omega^2 & -k_{mi} \\ -k_{mi} & k_{mi} - M_{MI}\omega^2 \end{bmatrix} \begin{bmatrix} X_{ma} \\ X_{mi} \end{bmatrix} = \begin{bmatrix} 0 \\ F \end{bmatrix}, \tag{35}$$

$$Z_{horz}(\omega) = \frac{1}{i\omega} \begin{bmatrix} k_{ma} + k_{mi} - M_{MA}\omega^2 & -k_{mi} \\ -k_{mi} & k_{mi} - M_{MI}\omega^2 \end{bmatrix}. \tag{36}$$

Figure 13 illustrates the main modeling parameters implemented for the marionette and mirror suspensions. This conservative approach reduces computational effort, as results from KAGRA [94] show that including the temperature gradients along the suspensions in the STN model has a negligible impact.

VI. SENSITIVITY OF THE BASELINE DESIGN

Using the STN model of Sec. V with the parameters in Tables II and III, the STN curves of the baseline design options are depicted in Fig. 14. Both the monocrystalline and the He-II–filled marionette suspension concepts fulfill the sensitivity requirements of the ET-D curve [2]. The combination of a He-II–filled marionette suspension with a sapphire mirror yields STN values similar to the monolithic sapphire marionette concept and is therefore not displayed.

When comparing the three STN curves of the baseline design in Fig. 14 with the suspension losses from Eq. (7), plotted for various materials in Fig. 15, two major conclusions can be drawn:

(1) The suspension loss angle ϕ_{susp}, especially of the mirror suspensions, has a crucial impact on the STN, yielding the difference between silicon and sapphire in the monocrystalline concepts.
(2) The lower marionette suspension temperature T_{ma} compensates higher marionette suspension losses ϕ_{susp} in the He-II–filled titanium suspension tube, yielding results similar to the monocrystalline silicon suspension concept in the range of 3 Hz to 30 Hz.

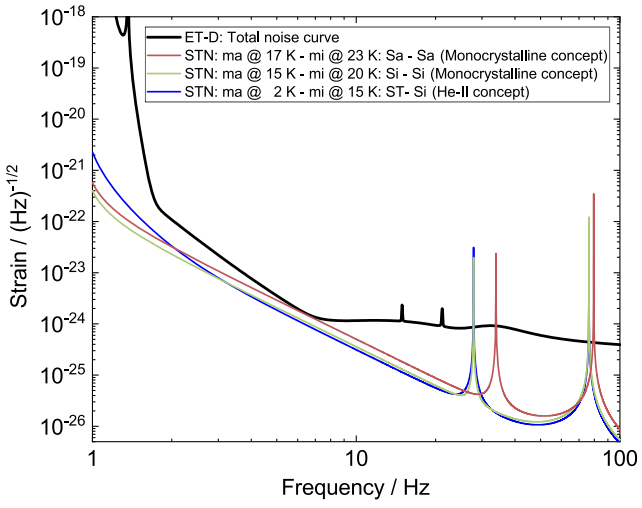

FIG. 14. STN of the baseline design for the monocrystalline and He-II–based marionette cooling concepts (Sa = sapphire, Si = silicon, ST = He-II suspension tube).

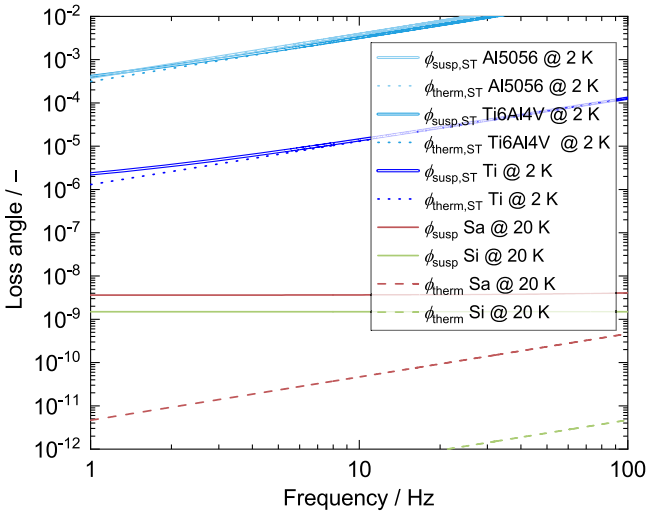

FIG. 15. ϕ_{susp} [Eq. (7)] and ϕ_{therm} [Eq. (8)] of the marionette suspension for metallic suspension tubes (ST) and for monolithic silicon and sapphire suspensions, with design parameters from Table II.

The latter effect can be deduced from the thermal noise of a simple harmonic oscillator far from its resonance (pendulum mode) at $\omega \gg \omega_0$ [12] as

$$S_{xx}(\omega) \propto T\phi_{susp}. \tag{37}$$

When approaching the pendulum peak $\omega \approx \omega_0$, however, the impact of ϕ_{susp} dominates the STN, which is visible at 1 Hz in Fig. 14.

Various values for the bulk loss angle ϕ_{bulk} of monocrystalline silicon and sapphire have been reported at cryogenic temperatures, see Table VII. This implies the necessity for R&D to refine the confidence interval of the data, which are immensely affected from the experimental setup. In this work, ϕ_{bulk} values of 1×10^{-9} and 3×10^{-9} have been applied for silicon and sapphire, respectively. Given the crucial influence of this parameter, as also presented in Sec. VII, these values should be revised accordingly based on future R&D.

The thermoelastic losses of silicon and sapphire at $T \leq 25$ K are negligible compared to the dominant bulk losses in ϕ_{susp}, as depicted for 20 K in Fig. 15. Further investigations on surface losses of treated, strength-improved monolithic silicon and sapphire crystals are crucial, in order to use reliable values in the model, because especially in small-scale structures such as suspensions, these losses can be a significant source [28,48]. For thin silicon flexures, Nawrodt *et al.* [48] report a surface loss parameter α_{surf} of 5×10^{-13} m at $T = 10$ K, yielding a dissipation depth of $h_s = 5 \times 10^{-4}$ m. For sapphire, currently the surface loss parameter has not been investigated; hence, it is assumed to be equal to that of silicon. In this model, for both silicon and sapphire suspensions, a value of $\alpha_{surf} = 5 \times 10^{-13}$ m is applied.

In the He-II concept, only losses in the titanium suspension tube are being considered so far. An additional contribution may originate from the static superfluid. Though the He-II dissipation is expected to be minor, this may change when the relative velocity between the two fluid components exceeds a critical value [95,96]. Above this critical velocity, a tangle of quantized vortices arises. Then an extra term, due to the interaction of the quantum vortices with the normal fluid should appear in addition to that of the viscous normal component. Since the ratio between the superfluid and the normal component is a function of temperature, the whole He-II contribution to the dissipation has to be investigated in future experiments, both in terms of frequency and temperature [97].

In metals, ϕ_{therm} represents the dominant loss contribution to ϕ_{susp}, cf. Fig. 15. Here, especially the parameters α and β are decisive. Compared to the other metals, titanium induces the lowest suspension losses, hence it is the proposed material for the suspension tube design. In this model, β_{Ti} is conservatively set equal to $\beta_{Ti6Al4V} = -4.6 \times 10^{-4}$, instead of -1.9×10^{-5} as reported in [98]. For the bulk losses, the conservative value of $\phi_{bulk} = 1 \times 10^{-6}$ at 2 K is used for the titanium suspension tube. A contribution from ϕ_{surf} is neglected, because the surface treatment and finishing technologies in metals are usually expected to provide a high-quality surface and hence a minor ϕ_{surf}. The cross-sectional area of the marionette suspension tube,

$$S_{ST} = \pi\left(\frac{d_o}{2} + s_o\right)^2 - \pi\left(\frac{d_o}{2}\right)^2, \tag{38}$$

is implemented in the evaluation of the tension in Eq. (8),

$$\sigma = \frac{M_{MA+MI}g}{S_{ST}}, \tag{39}$$

and converted to an equivalent diameter,

$$d_{ST} = \sqrt{\frac{4S_{ST}}{\pi}}, \tag{40}$$

to be applied in Eq. (9). The suspension tube area moment of inertia used in Eq. (14) is

$$I_{ST} = \frac{\pi}{4}\left[\left(\frac{d_o}{2} + s_o\right)^4 - \left(\frac{d_o}{2}\right)^4\right]. \tag{41}$$

VII. PARAMETER STUDY

A. General

This section presents a study of various payload design parameters that influence the STN in the ET-LF frequency range. We use the He-II–filled marionette suspension concept with a silicon mirror as a reference, because variations of other design parameters do not affect the temperature $T_{ma} = T_{MA} = 2$ K in this case. Therefore, effects of different mirror suspension designs can be better discriminated. The applied physical property data are summarized in Table III. For a consistent comparison, the analysis considers the resulting mirror temperatures $T_{mi} = T_{MI}$ due to the parameter variations—i.e., a mechanical dimensioning and a thermal modeling is applied prior to each STN modeling. The results of the parameter study are visualized in Figs. 16 and 17 in the frequency range of 0.3 Hz to 100 Hz in order to include the impact on the pendulum modes below 1 Hz.

B. Influence of the mirror suspension design

The mirror suspension design determines the STN in the frequency range above 10 Hz, especially due to the violin and the vertical modes, but it also impacts the sensitivity at lower frequencies. Variations of the mirror suspension temperature, length, diameter, and bulk losses are investigated.

With $T_{ma} = T_{MA} = 2$ K, the temperature $T_{mi} = T_{MI}$ is a function of the heat load. Around the design target from Eq. (1), heat loads of 0.1 W, 0.5 W, and 1.0 W yield silicon

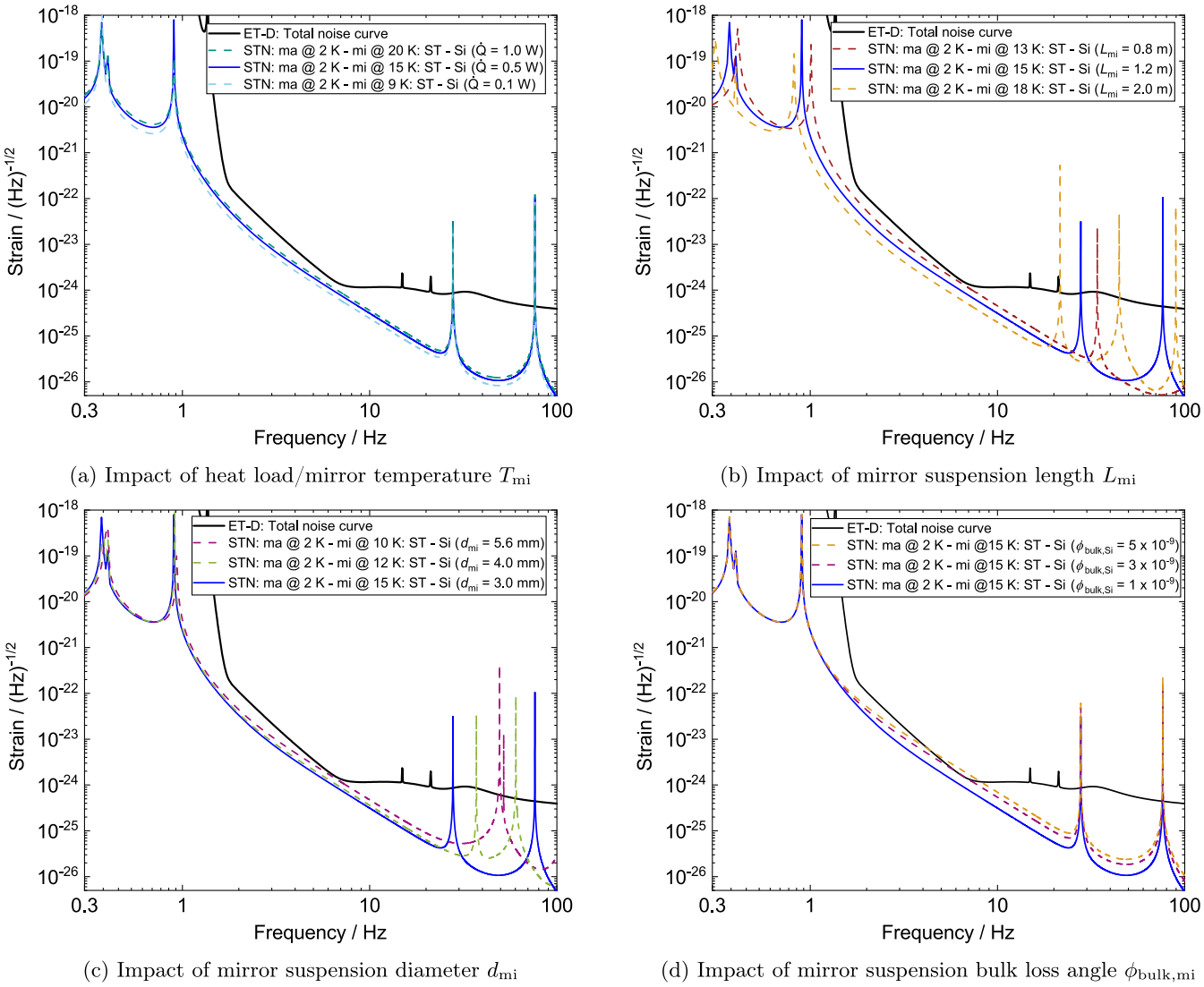

(a) Impact of heat load/mirror temperature T_{mi}

(b) Impact of mirror suspension length L_{mi}

(c) Impact of mirror suspension diameter d_{mi}

(d) Impact of mirror suspension bulk loss angle $\phi_{\mathrm{bulk,mi}}$

FIG. 16. Sensitivity analyses of the mirror suspension parameters T_{mi}, L_{mi}, d_{mi}, and $\phi_{\mathrm{bulk,mi}}$ on the STN.

mirror temperatures of 9 K, 15 K, and 20 K, respectively. The corresponding STN curves in Fig. 16(a) indicate a minor effect of the heat load on the STN. It must be noted, however, that the achievable mirror temperature strongly depends on the marionette temperature.

The length of the mirror suspensions is an essential design parameter, influencing both the STN and the cryostat design. Figure 16(b) shows the STN for mirror suspensions of 2.0 m, 1.2 m, and 0.8 m length, yielding mirror temperatures of 18 K, 15 K, and 13 K, respectively, at 0.5 W heat load. A decreasing length L_{mi} yields a shift of all the modes to higher frequencies. This is beneficial for the sensitivity regrading the violin and vertical modes, but it also implies a shift of the pendulum modes below 1 Hz to higher frequencies. The latter results in an STN increase from 1 Hz to 20 Hz. Therefore, L_{mi} is a design parameter to be optimized, considering constraints imposed by the ET-LF sensitivity, ongoing R&D on high-quality fiber manufacturing [50], and the ET-LF cryostat and tower dimensions.

The impact of the mirror suspension diameter d_{mi} is presented in Fig. 16(c), considering different ultimate strength values and mechanical safety factors. Measured ultimate strength values of silicon at cryogenic temperatures lie between 230 MPa [28] and 120 MPa [99]. In order to consider mechanical strength uncertainties related to silicon jointing methods, the application of a safety factor of 3 or 6 is foreseen in the parameter study. This yields $d_{\mathrm{mi}} = 3$ mm for $\sigma_{\mathrm{max}} = 230$ MPa with SF $= 3$, $d_{\mathrm{mi}} = 4$ mm for $\sigma_{\mathrm{max}} = 120$ MPa with SF $= 3$, and $d_{\mathrm{mi}} = 5.6$ mm for $\sigma_{\mathrm{max}} = 120$ MPa with SF $= 6$. Increasing suspension diameters d_{mi} result in higher STN values, despite a better heat

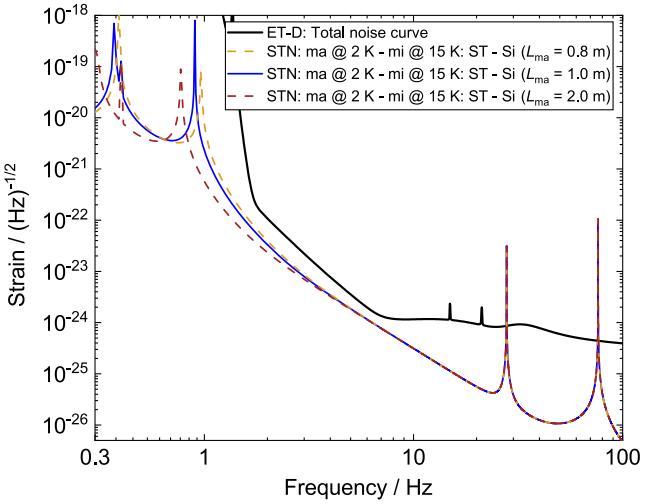

(a) Impact of marionette suspension length L_{ma}

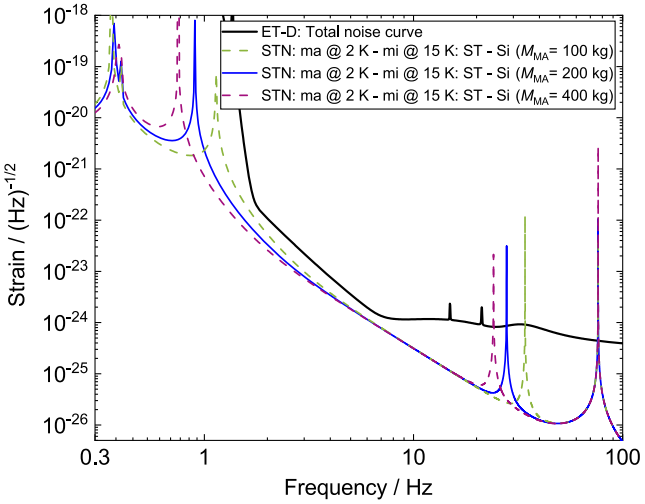

(b) Impact of marionette mass M_{MA}

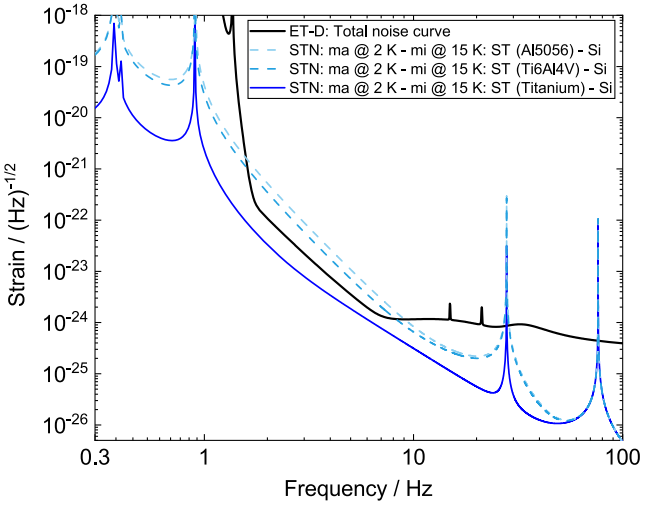

(c) Impact of marionette suspension tube material

FIG. 17. Parameter analysis of the marionette design parameters: L_{ma}, M_{MA}, $\phi_{\mathrm{susp,ma}}$ on the STN.

extraction with lower temperatures T_{mi}. This is mainly caused by the shifting of the vertical and first violin modes toward each other. Furthermore, d_{mi} determines the position of the mirror suspension bending points via $\lambda_{\mathrm{bp}} = \sqrt{EI/\sigma}$, which due to payload-control-related constraints must be aligned with the center of mass of the suspended mirror and marionette. As a consequence, the overall length of the mirror suspensions must include these additional lengths in the upper and lower parts. For the baseline design parameters in Table II, both sapphire and silicon yield a total additional length of 6 cm. This additional length has a negligible impact on the STN modeling, but it is an important aspect to be considered in the suspension manufacturing and payload design, such as the calculation of the suspension system frequencies and temperature gradients.

The mirror suspension bulk loss angle $\phi_{\mathrm{bulk,mi}}$ has a strong impact on the STN, given that it directly affects the overall mechanical dissipation of the suspensions, cf. Eq. (7). Figure 16(d) shows the STN for silicon mirror suspensions with $\phi_{\mathrm{bulk,mi}}$ values of 1×10^{-9}, 3×10^{-9}, and 5×10^{-9}. The surface losses are calculated under the assumption of a constant dissipation depth of $h_s = 5 \times 10^{-4}$ m according to Eq. (10), yielding total suspension losses $\phi_{\mathrm{susp,mi}}$ of 2.3×10^{-9}, 7×10^{-9}, and 1.2×10^{-8}, respectively. Increasing $\phi_{\mathrm{bulk,mi}}$ induces a higher STN over the complete frequency range.

C. Influence of the marionette suspension design

The marionette suspension has a dominant impact on the STN at frequencies below 10 Hz. Again, we use the He-II–filled marionette suspension concept for reference, where $T_{\mathrm{ma}} = T_{\mathrm{MA}} = 2$ K is fixed on principle, and we investigate the influence of the suspension length, the marionette mass, and the suspension material. The resulting trends may apply to monolithic marionette suspensions as well, but more detailed design studies including the cooling interface will be necessary in order to determine appropriate temperature values.

Figure 17(a) presents the STN modeled with marionette suspension lengths of $L_{\mathrm{ma}} = 0.8$ m, 1.0 m, and 2.0 m. A decrease in L_{ma} yields a shift of the pendulum modes to higher frequencies. Increasing STN values, however, are only observed at $f < 3$ Hz. The violin and the vertical modes remain unchanged, as they are defined solely by the mirror suspensions.

The variation of STN with marionettes of 100 kg, 200 kg, and 400 kg is analyzed in Fig. 17(b). A reduction of the marionette mass results in a shift of the pendulum and the vertical modes to higher frequencies, resulting in slightly higher STN values in the frequency range of 3 Hz to 5 Hz. The benefit of a lighter marionette, however, is a reduced cooldown time. Additional restrictions may come

from the payload control system, whereby the marionette should not weigh less than the mirror.

The marionette suspension tube material influences the STN via the suspension losses ϕ_{susp} (cf. Fig. 15) and the wall thickness resulting from the mechanical dimensioning. Figure 17(c) depicts the impact of different materials on the STN, showing that the ET-D sensitivity curve can only be reached with a titanium suspension tube.

VIII. CONCLUSIONS AND OUTLOOK

We presented a baseline design for the ET-LF cryogenic payload, which is thermally and mechanically consistent and fulfils the STN requirements given by the ET-D sensitivity curve. Analytic and FEA simulations indicate that soft thermal links cannot be connected to the marionette. Therefore, two possible heat extraction concepts are proposed, including a high-Q and high-conductivity monocrystalline marionette suspension made of silicon or sapphire, and a He-II–filled marionette suspension tube made of titanium. In the latter case, the lower operating temperature of 2 K compensates for the lower Q of titanium. The theoretical fundamentals of STN modeling applied to cryogenic payloads are described in detail, and available sources for material data are compiled. A parameter study is performed in order to identify the impact of various design parameters on the ET-LF sensitivity, illustrating the parameter space for future payload design optimizations. The suspension losses are shown to have a decisive impact, highlighting the need for dedicated R&D on bulk and surface losses under ET-LF operating conditions. A reduction of the mirror suspension length is shown to deteriorate the STN in the ET-LF frequency range, whereas the marionette suspension length has a less important impact. Hence, a combined variation of these two parameters may be beneficial in future design studies. The actual value of the heat load on the mirror is shown to have a marginal impact on the STN, assuming that the necessary cooling capacity is available.

Future R&D on cryogenic payloads will be embedded in a wide context of activities outlined, e.g., in [100]. For the monocrystalline concept foreseeing a silicon or sapphire marionette suspension, the cooldown behavior and vibration transmission will be investigated in upcoming R&D in the ET-Cryo facility of the Amaldi Research Center (ARC), devoted to testing and developing the main features of an ET-LF payload using a solid conductive cooling cryostat. Thermal shielding and soft thermal links, as well as high-Q and high-conductivity monocrystalline suspensions for the marionette and mirror will be tested. Also, key relevant features concerning the cryostat design versus payload will be tested in order to envisage the actual impact of connecting the payload to the cryogenic system. The ARC ET-Cryo Lab is ready, and the design of the test cryostat is underway. The alternative He-II concept is shown to fulfill the STN requirements as well, cooling the marionette to 2 K and conducting the heat load through a static He-II column inside the marionette suspension tube. This concept enables convective cooldown of the ET-LF payload by controlled He-I flow in about two weeks. Open questions related to the integration of a quantum fluid in a gravitational wave detector suspension—in particular, the effect of He-II on mechanical dissipation and vibration transmission—will be addressed in future experiments by the authors at KIT. A new facility for Q measurements down to 2 K is presently being planned, allowing investigations of both solid and He-II–filled suspensions. The scope of this facility includes R&D on the mechanical integration of the cooling interface on the platform, the supply capillaries, and their vibration attenuation system in order to investigate the noise propagation from the cooling system into the payload.

ACKNOWLEDGMENTS

The authors would like to acknowledge the support from the German Ministry for Education and Research (BMBF, Gr 05A20VK4), and from the Karlsruhe School of Elementary Particle and Astroparticle Physics: Science and Technology (KSETA). The study in this paper has been developed within the frameworks of Italian PRIN2020, cod. 2020BSYXCB LoVeC-ET (Low-frequency Versus Cryogenics for ET), the EC exchange program NEWS—H2020-MSCA-RISE-2016 GA No. 734303, and the ETIC—Einstein Telescope Infrastructure Consortium (IR0000004)—MUR call No. 3264 PNRR, Miss.4—Comp. 2, Line 3.1. We are indebted to KAGRA colleagues for the precious discussions concerning solid conduction cooling down of payloads.

SYMBOL LIST

Symbol	Definition
α	Linear expansion coefficient
α	Heat transfer coefficient
α_{surf}	Surface loss parameter
β	Thermal elastic coefficient
ϵ	Effective emissivity
λ	Thermal conductivity
λ_{bp}	Bending point position
μ	Geometry factor
ρ	Density
η	Dynamic viscosity
ω	Angular frequency
σ	Tension
σ_{max}	Ultimate tensile strength
σ_{y}	Yield strength
τ	Thermal diffusion time
ϕ	Loss angle
A	Area
A_{surf}	Surface area
C	Constant
c_{p}	Specific heat capacity
d	Diameter
D	Dilution factor
E	Young's modulus
f	Frequency
F	Force
g	Standard gravitational acceleration
h	Height
h_{s}	Dissipation depth
I	Area moment of inertia
k	Spring constant
k_{B}	Boltzmann constant
k_{e}	Elastic fiber wave number
k_{s}	Flexural stiffness wave number
L	Length
$\dot{M}$	Mass flow
M	Mass
n	Number of fibers
p	Pressure
$\dot{q}$	Heat flux
$\dot{Q}$	Cooling power
Q	Quality factor
s	Specific entropy
s	Wall thickness
S	Cross-sectional area
S_{xx}	Displacement spectral density
t	Time
T	Temperature
V	Volume
x	Displacement in the time domain
X	Displacement in the frequency domain
y	Longitudinal coordinate
Y	Mechanical admittance
Z	Mechanical impedance
†	Complex conjugate and transposed matrix

ABBREVIATION LIST

Abbreviation	Definition
Al	Aluminium alloy 1200
CA	Cage
CFD	Computational fluid dynamics
DoF	Degree of freedom
el	Elastic
cx	Complex
ET	Einstein Telescope
FDT	Fluctuation dissipation theorem
g	Gravitational
GW	Gravitational wave
HCB	Hydroxide catalysis bonding
h	Hydraulic
horz	Horizontal
HF	High frequency
HT	Heat transfer
i	Inner
in	Inlet
join	Jointing
LF	Low frequency
MA	Marionette
ma	Marionette suspension
MI	Mirror
mi	Mirror suspension
PF	Platform
pend	Pendulum
o	Outer
out	Outlet
RRR	Residual resistivity ratio
Sa	Sapphire
Si	Silicon
SF	Safety factor
surf	Surface
susp	Suspension
ST	Suspension tube
STN	Suspension thermal noise
therm	Thermoelastic
Ti	Titanium
TL	Thermal link
vert	Vertical

[1] M. Branchesi *et al.*, Science with the Einstein Telescope: A comparison of different designs, J. Cosmol. Astropart. Phys. 07 (2023) 068.

[2] ET Science Team, Einstein Gravitational Wave Telescope conceptual design study (2011), https://apps.et-gw.eu/tds/?content=3&r=8709.

[3] F. Basti, F. Frasconi, E. Majorana, L. Naticchioni, M. Perciballi, P. Puppo, P. Rapagnani, and F. Ricci, A cryogenic payload for the 3rd generation of gravitational wave interferometers, Astropart. Phys. **35**, 67 (2011).

[4] P. Puppo, X. Koroveshi, E. Majorana, P. Rapagnani, and S. Grohmann, Update on the suspension thermal noise modelling of the ET-LF cryogenic payload, *Talk Held at ECLOUD and GWDVac'22 Workshops, Portoferraio, Italy* (2022), 10.5445/IR/1000153746.

[5] ET Steering Committee, Design Report Update 2020 for the Einstein Telescope (2020), https://apps.et-gw.eu/tds/ql/?c=15418.

[6] K. Yamamoto, Playload design at KAGRA and its impact to vacuum and cryogenics, *Talk Held at ECLOUD and GWDVac'22 Workshops, Portoferraio, Italy* (2022).

[7] L. Naticchioni (Virgo Collaboration), The payloads of Advanced Virgo: Current status and upgrades, J. Phys. Conf. Ser. **957**, 012002 (2018).

[8] E. Majorana, Outline of cryogenic payload compliance with Einstein Telescope LF, *Talk Held at GWADW* (2021).

[9] P. Puppo, FEA models for the ET payload: Status and preliminary results, *Talk Held at GWADW* (2022), https://apps.et-gw.eu/tds/ql/?c=16309.

[10] T. Sumomogi, M. N. Masashi Yoshida, H. Osono, and T. Kino, Mechanical properties of ultra high-purity aluminum, J. Jpn. Inst. Metals **68**, 958 (2004).

[11] R. Nawrodt *et al.*, High mechanical *Q*-factor measurements on silicon bulk samples, J. Phys. Conf. Ser. **122**, 012008 (2008).

[12] P. R. Saulson, Thermal noise in mechanical experiments, Phys. Rev. D **42**, 2437 (1990).

[13] A. S. Nowick and B. S. Berry, *Anelastic Relaxation in Crystalline Solids* (Academic Press, New York, 1972).

[14] T. Yamada, T. Tomaru, T. Suzuki, T. Ushiba, N. Kimura, S. Takada, Y. Inoue, and T. Kajita, High performance thermal link with small spring constant for cryogenic applications, Cryogenics **116**, 103280 (2021).

[15] T. Yamada, Reduction of vibration transfer via heat links in KAGRA cryogenic mirror suspension system, *Talk Held at GWADW* (2021).

[16] T. Ushiba *et al.*, Cryogenic suspension design for a kilometer-scale gravitational-wave detector, Classical Quantum Gravity **38**, 8 (2021).

[17] P. Ruggi, Mechanical noise in gravitational wave detectors, *Talk Held at Amaldi Research Center Summer School, Paestum, Italy* (2022).

[18] A. Dari, F. Travasso, H. Vocca, and L. Gammaitoni, Breaking strength tests on silicon and sapphire bondings for gravitational wave detectors, Classical Quantum Gravity **27**, 045010 (2010).

[19] M. Phelps, M. M. Reid, R. Douglas, A.-M. van Veggel, V. Mangano, K. Haughian, A. Jongschaap, M. Kelly, J. Hough, and S. Rowan, Strength of hydroxide catalysis bonds between sapphire, silicon, and fused silica as a function of time, Phys. Rev. D **98**, 122003 (2018).

[20] E. R. Dobrovinskaya, L. A. Lytvynov, and V. Pishchik, Properties of sapphire, in *Sapphire: Material, Manufacturing, Applications* (Springer US, Boston, 2009), pp. 55–176.

[21] T. Yamada, Sapphire bending tests, Public and Internal note database at Institute for Cosmic Ray Research (ICRR) University of Tokyo, Report No. JGW-T2314883-v1, 2023.

[22] SHINKOSHA CO., LTD. 2-4-1 Kosugaya, Sakae-ku, Yokohama, Kanagawa 247-0007 Japan.

[23] D. F. McGuigan, C. C. Lam, R. Q. Gram, A. W. Hoffman, D. H. Douglass, and H. W. Gutche, Measurements of the mechanical *Q* of single-crystal silicon at low temperatures, J. Low Temp. Phys. **30**, 621 (1978).

[24] C. R. Locke, M. E. Tobar, and E. N. Ivanov, Properties of a monolithic sapphire parametric transducer: Prospects of measuring the standard quantum limit, Classical Quantum Gravity **19**, 1877 (2002).

[25] S. Amadori, E. Bonetti, L. Pasquini, P. Deodati, R. Donnini, R. Montanari, and C. Testani, Low temperature anelasticity in Ti6Al4V alloy and Ti6Al4V-SiCf composite, Mater. Sci. Eng. **521–522**, 340 (2009).

[26] W. Duffy, Acoustic quality factor of titanium from 50 mK to 300 K, Cryogenics **40**, 417 (2000).

[27] W. Duffy, Acoustic quality factor of aluminium and selected aluminium alloys from 50 mK to 300 K, Cryogenics **42**, 245 (2002).

[28] A. V. Cumming *et al.*, Silicon mirror suspensions for gravitational wave detectors, Classical Quantum Gravity **31**, 025017 (2013).

[29] J. W. Ekin, *Experimental Techniques for Low-Temperature Measurements: Cryostat Design, Material Properties and Superconductor Critical-Current Testing* (Oxford University Press, Oxford, UK, 2006).

[30] Y. S. Touloukian, R. W. Powell, C. Y. Ho, and P. G. Klemens, Thermophysical properties of matter—the TPRC data series: Volume 1. Thermal conductivity—metallic elements and alloys. Data book (1970).

[31] A. Khalaidovski *et al.*, Evaluation of heat extraction through sapphire fibers for the GW observatory KAGRA, Classical Quantum Gravity **31**, 105004 (2014).

[32] CryoData Inc., CryoComp, Data from: NIST—Properties of solid materials from cryogenic- to room-temperatures (1999).

[33] B. Baudouy and A. Four, Low temperature thermal conductivity of aluminum alloy 5056, Cryogenics **60**, 1 (2014).

[34] Y. S. Touloukian and E. H. Buyco, Thermophysical properties of matter—the TPRC data series: Volume 4. Specific heat—metallic elements and alloys. Data book (1971).

[35] G. K. White and M. L. Minges, Thermophysical properties of some key solids: An update, Int. J. Thermophys. **18**, 1269 (1997).

[36] M. Barucci, C. Ligi, L. Lolli, A. Marini, V. Martelli, L. Risegari, and G. Ventura, Very low temperature specific heat of Al 5056, Physica (Amsterdam) **405B**, 1452 (2010).

[37] C. A. Swenson, Recommended values for the thermal expansivity of silicon from 0 to 1000 K, J. Phys. Chem. Ref. Data **12**, 179 (1983).

[38] C. Taylor, M. Notcutt, E. Wong, A. Mann, and D. Blair, Measurement of the coefficient of thermal expansion of a cryogenic, all-sapphire, Fabry-Perot optical cavity, Opt. Commun. **131**, 311 (1996).

[39] Y. S. Touloukian, R. K. Kirby, R. E. Taylor, and P. D. Desai, Thermophysical properties of matter—the TPRC data series: Volume 12. Thermal expansion metallic elements and alloys. Data book (1975).

[40] U. Gysin, S. Rast, P. Ruff, E. Meyer, D. W. Lee, P. Vettiger, and C. Gerber, Temperature dependence of the force sensitivity of silicon cantilevers, Phys. Rev. B **69**, 045403 (2004).

[41] J. B. Wachtman Jr., W. E. Tefft, D. G. Lam Jr., and C. S. Apstein, Exponential temperature dependence of Young's modulus for several oxides, Phys. Rev. **122**, 1754 (1961).

[42] M. Fukuhara and A. Sanpei, Elastic moduli and internal frictions of Inconel 718 and Ti-6Al-4V as a function of temperature, J. Mater. Sci. Lett. **12**, 1122 (1993).

[43] National Institute of Standards and Technology (NIST), Properties of solid materials from cryogenic- to room-temperatures.

[44] M. A. Hopcroft, W. D. Nix, and T. W. Kenny, What is the young's modulus of silicon? J. Microelectromech. Syst. **19**, 229 (2010).

[45] J. B. Wachtman Jr. and D. G. Lam Jr., Young's modulus of various refractory materials as a function of temperature, J. Am. Ceram. Soc. **42**, 254 (1959).

[46] R. R. Boyer, G. Welsch, and E. W. Collings, *Materials Properties Handbook: Titanium Alloys* (ASM International, Materials Park, Ohio, 1994).

[47] R. Nawrodt *et al.*, Mirror thermal noise calculation for ET (2009), https://apps.et-gw.eu/tds/ql/?c=7556.

[48] R. Nawrodt *et al.*, Investigation of mechanical losses of thin silicon flexures at low temperatures, Classical Quantum Gravity **30**, 115008 (2013).

[49] R. G. Scurlock, *Low Temperature Behaviour of Solids* (Routledge and Kegan Paul PLC, London, 1966).

[50] F. Travasso *et al.*, Towards a silicon monolithic suspension, *Proceedings of the 2nd Gravitational-Waves Science & Technology Symposium (GRASS), Padova, Italy* (2019).

[51] A. Sato, M. Maeda, T. Dantsuka, M. Yuyama, and Y. Kamioka, Temperature dependence of the Gorter-Mellink exponent m measured in a channel containing He II, AIP Conf. Proc. **823**, 387 (2006).

[52] CryoData Inc., HEPAK, Data from: V. D. Arp, R. D. Mccarty and D. G. Friend—Thermophysical properties of helium-4 from 0.8 to 1500 K with pressures to 2000 MPa (1998), https://htess.com/hepak/.

[53] Y. S. Touloukian, R. W. Powell, C. Y. Ho, and P. G. Klemens, Thermophysical properties of matter—The TPRC data series: Volume 2. Thermal conductivity—Nonmetallic solids. Data book (1971).

[54] P. Astone *et al.*, Noise behaviour of the explorer gravitational wave antenna during λ transition to the superfluid phase, Cryogenics **32**, 668 (1992).

[55] P. Puppo and F. Ricci, Cryogenics and Einstein telescope, Gen. Relativ. Gravit. **43**, 657 (2011).

[56] W. F. Vinen, The physics of superfluid helium (2004).

[57] S. W. Van Sciver, *Helium Cryogenics*, 2nd ed., International Cryogenics Monograph Series (Springer, New York, NY, 2012).

[58] L. Landau, Theory of the superfluidity of helium II, Phys. Rev. **60**, 356 (1941).

[59] L. Tisza, Transport phenomena in helium II, Nature (London) **141**, 913 (1938).

[60] T. Yamada (KAGRA Collaboration), KAGRA cryogenic suspension control toward the observation run 3, J. Phys. Conf. Ser. **1468**, 012217 (2020).

[61] L. Busch and S. Grohmann, Conceptual layout of a helium cooling system for the Einstein telescope, IOP Conf. Ser. **1240**, 012095 (2022).

[62] L. Busch and S. Grohmann, Thermal design of the He-II suspension tube for ET-LF: Status and outlook, *Talk Held at ECLOUD and GWDVac Workshops, Portoferraio, Italy* (2022), 10.5445/IR/1000153741.

[63] L. Busch, X. Koroveshi, and S. Grohmann, Helium-based cooling concept of the ET-LF interferometer, *Talk Held at the Gravitational Wave Advanced Detector Workshop (GWADW), Online* (2021), 10.5445/IR/1000132799.

[64] B. Baudouy, Low temperature thermal conductivity of aluminum alloy 1200, Cryogenics **51**, 617 (2011).

[65] E. Lemmon, M. Huber, and M. McLinden, NIST Standard Reference Database 23: Reference Fluid Thermodynamic and Transport Properties—REFPROP, Version 9.1 (2013).

[66] C. H. Twu, J. E. Coon, and J. R. Cunningham, A new generalized alpha function for a cubic equation of state: Part 1. Peng-Robinson equation, Fluid Phase Equilib. **105**, 49 (1995).

[67] V. Yakhot and S. A. Orszag, Renormalization group analysis of turbulence: I. Basic theory, J. Sci. Comput. **1**, 3 (1986).

[68] J. Abrahamson, Ansys Fluent Theory Guide (2022), release 2022 R1.

[69] M. Constancio Jr, R. X. Adhikari, O. D. Aguiar, K. Arai, A. Markowitz, M. A. Okada, and C. C. Wipf, Silicon emissivity as a function of temperature, Int. J. Heat Mass Transfer **157**, 119863 (2020).

[70] P. D. Desai, Thermodynamic properties of iron and silicon, J. Phys. Chem Ref. Data **15**, 967 (1986).

[71] H. B. Callen and T. A. Welton, Irreversibility and generalized noise, Phys. Rev. **83**, 34 (1951).

[72] P. R. Saulson, *Fundamentals of Interferometric Gravitational Wave Detectors* (World Scientific, Singapore, 1994).

[73] Y. Levin, Internal thermal noise in the LIGO test masses: A direct approach, Phys. Rev. D **57**, 659 (1998).

[74] G. I. González and P. R. Saulson, Brownian motion of a mass suspended by an anelastic wire, J. Acoust. Soc. Am. **96**, 207 (1994).

[75] G. González, Suspensions thermal noise in the LIGO gravitational wave detector, Classical Quantum Gravity **17**, 4409 (2000).

[76] E. Majorana and Y. Ogawa, Mechanical thermal noise in coupled oscillators, Phys. Lett. A **233**, 162 (1997).

[77] G. Cagnoli, J. Hough, D. DeBra, M. Fejer, E. Gustafson, S. Rowan, and V. Mitrofanov, Damping dilution factor for a pendulum in an interferometric gravitational waves detector, Phys. Lett. A **272**, 39 (2000).

[78] S. Rowan, G. Cagnoli, P. Sneddon, J. Hough, R. Route, E. Gustafson, M. Fejer, and V. Mitrofanov, Investigation of mechanical loss factors of some candidate materials for the test masses of gravitational wave detectors, Phys. Lett. A **265**, 5 (2000).
[79] A. Schröter, Dissertation: Mechanical losses in materials for future cryogenic gravitational wave detectors (2008).
[80] V. B. Braginsky, V. Mitrofanov, and V. I. Panov, *Systems with Small Dissipation* (University of Chicago Press, Chicago, 1985).
[81] T. Uchiyama *et al.*, Mechanical quality factor of a cryogenic sapphire test mass for gravitational wave detectors, Phys. Lett. A **261**, 5 (1999).
[82] E. Majorana, P. Rapagnani, and F. Ricci, Test facility for resonance transducers of cryogenic gravitational wave antennas, Meas. Sci. Technol. **3**, 501 (1992).
[83] W. Duffy, Acoustic quality factor of aluminum alloys from 50 mK to 300 K, J. Appl. Phys. **68**, 5601 (1990).
[84] E. Coccia and T. Niinikoski, Acoustic quality factor of an aluminium alloy for gravitational wave antennae below 1 K, Lett. Nuovo Cimento **41**, 242 (1984).
[85] P. Astone *et al.*, Long-term operation of the Rome "explorer" cryogenic gravitational wave detector, Phys. Rev. D **47**, 362 (1993).
[86] C. Zener, Internal friction in solids: II. General theory of thermoelastic internal friction, Phys. Rev. **53**, 90 (1938).
[87] G. Cagnoli and P. A. Willems, Effects of nonlinear thermoelastic damping in highly stressed fibers, Phys. Rev. B **65**, 174111 (2002).
[88] R. Nawrodt, S. Rowan, J. Hough, M. Punturo, F. Ricci, and J. Vinet, Challenges in thermal noise for 3rd generation of gravitational wave detectors, Gen. Relativ. Gravit. **43**, 593 (2011).
[89] A. M. Gretarsson, G. M. Harry, S. D. Penn, P. R. Saulson, W. J. Startin, S. Rowan, G. Cagnoli, and J. Hough, Pendulum mode thermal noise in advanced interferometers: A comparison of fused silica fibers and ribbons in the presence of surface loss, Phys. Lett. A **270**, 108 (2000).
[90] A. V. Cumming, B. Sorazu, E. Daw, G. D. Hammond, J. Hough, R. Jones, I. W. Martin, S. Rowan, K. A. Strain, and D. Williams, Lowest observed surface and weld losses in fused silica fibres for gravitational wave detectors, Classical Quantum Gravity **37**, 195019 (2020).
[91] F. Piergiovanni, M. Punturo, and P. Puppo, The thermal noise of the Virgo+ and Virgo Advanced Last Stage Suspension (The PPP Effect) (2009), https://tds.virgo-gw.eu/ql/?c=2199.
[92] K. Somiya, Suspension thermal noise reduction in a cryogenic interferometer (2011).
[93] F. Bondu, P. Hello, and J. Vinet, Thermal noise in mirrors of interferometric gravitational wave antennas, Phys. Lett. A **246**, 227 (1998).
[94] K. Komori, Y. Enomoto, H. Takeda, Y. Michimura, K. Somiya, M. Ando, and S. W. Ballmer, Direct approach for the fluctuation-dissipation theorem under nonequilibrium steady-state conditions, Phys. Rev. D **97**, 102001 (2018).
[95] C. J. Gorter and J. Mellik, On the irreversible processes in liquid helium II, Physica **15**, 285 (1949).
[96] R. P. Feynman, Application of quantum mechanics to liquid helium, in *Progress in Low Temperature Physics*, edited by C. J. Gorter (North-Holland Publications, Amsterdam, 1955), Vol. 1, pp. 17–53.
[97] X. Koroveshi, S. Grohmann, P. Rapagnani, and V. Mangano, Experimental plans to validate the He-II based payload cooling concept, *Talk Held at ECLOUD and GWDVac'22 Workshops, Portoferraio, Italy* (2022), 10.5445/IR/1000153742/v2.
[98] E. S. Fisher and C. J. Renken, Single-crystal elastic moduli and the hcp → bcc transformation in Ti, Zr, and Hf, Phys. Rev. **135**, A482 (1964).
[99] Core Optics and Suspensions working group, Silicon suspensions for ET-LF, in *Talk held in Einstein Telescope—ISB Workshop, L'Aquila, Italy* (2022).
[100] S. Di Pace *et al.*, Research facilities for Europe's next generation gravitational-wave detector Einstein telescope, Galaxies **10**, 1 (2022).